

## ORIGINAL ARTICLE

# Garnet growth and mineral geochronology constrains the diachronous Neoproterozoic convergent evolution of the southern Dom Feliciano Belt, Uruguay

Jack James Percival<sup>1</sup>  | Jiří Konopásek<sup>1,2</sup>  | Pedro Oyhantçabal<sup>3</sup> |  
Jiří Sláma<sup>4</sup>  | Robert Anczkiewicz<sup>5</sup> 

<sup>1</sup>Department of Geosciences, UiT–The Arctic University of Norway, Tromsø, Norway

<sup>2</sup>Czech Geological Survey, Prague, Czech Republic

<sup>3</sup>Departamento de Geodinámica Interna, Facultad de Ciencias, Universidad de La República, Montevideo, Uruguay

<sup>4</sup>Institute of Geology of the Czech Academy of Sciences, Prague, Czech Republic

<sup>5</sup>Institute of Geological Sciences, Polish Academy of Sciences, Kraków Research Centre, Kraków, Poland

## Correspondence

Jack James Percival, Department of Geosciences, UiT–The Arctic University of Norway, Dramsvæien 201, 9037, Tromsø, Norway.

Email: [jack.j.perc@gmail.com](mailto:jack.j.perc@gmail.com)

Handling Editor: Dr. Bernardo Cesare

## Funding information

Coordination for the Improvement of Higher Education Personnel (CAPES), Grant/Award Number: UTF-2018-10004; Czech Science Foundation, Grant/Award Number: 18-24281S; Norwegian Agency for International Cooperation and Quality Enhancement in higher Education (Diku)

## Abstract

The Dom Feliciano Belt of southern Brazil and Uruguay represents part of a larger Neoproterozoic orogenic system formed during the amalgamation of Western Gondwana. The hinterland and foreland domains in parts of the belt preserve deformation structures and metamorphic assemblages that developed during early crustal thickening from c. 650 Ma. However, the metamorphic history of the southern foreland, in Uruguay, and its relationship with the hinterland, is not so well understood. We show that metamorphism in the southern hinterland is characterized by near-isothermal decompression from ~10 kbar (~770°C) down to ~6 kbar, reflecting exhumation from depths of ~40 km during convergent thrusting and crustal thickening. This metamorphic event and associated magmatism is constrained by garnet Lu–Hf and zircon U–Pb dating to c. 655–640 Ma, supporting age and P–T constraints from previous studies. In contrast, prograde metamorphism in the foreland supracrustal rocks reached maximum lower-amphibolite facies conditions (~6–7 kbar and ~550–570°C) and is constrained by garnet Lu–Hf dating to  $582 \pm 23$  Ma. An exposed sheet of imbricated foreland basement rocks reached partial melting at upper-amphibolite facies conditions, and metamorphism is similarly constrained to c. 585–570 Ma by monazite U–Pb dating. The data indicate that metamorphism in the foreland occurred during a sinistral transpressional event c. 55–85 Ma after the start of crustal thickening recorded in the hinterland, whereby strain partitioning during sinistral transpression led to imbrication in the foreland and oblique thrusting of the basement over more distal supracrustal rocks. This event is coeval with transpressional deformation in the Kaoko and Gariep belts, indicating a distinct two-stage tectonic history driven by the three-way convergence between the Congo, Kalahari, and South American cratons.

# 1 | INTRODUCTION

The exhumed roots of orogenic belts and their interactions with foreland domains reveal fundamental details about the evolution of orogenic crustal thickening, and assessing the nature of these events requires the integration of structural and metamorphic petrological observations with geochronological data (e.g., Meira et al., 2019; Percival et al., 2022; Tajčmanová et al., 2006). Correlating the growth of dated minerals with specific structures and tectonic events allows the construction of P–T–t paths, which can then be used to interpret the development of orogens on a large scale (e.g., Coelho et al., 2017; Goscombe et al., 2017, 2018; Larson et al., 2020; Schulmann et al., 2009).

The Dom Feliciano Belt, outcropping in southern Brazil and Uruguay, is part of the larger South Atlantic Neoproterozoic Orogenic System (SANOS; Konopásek et al., 2020 Figure 1a). The belt represents the western half of a largely symmetric orogenic structure with a distinct two-stage evolution. Early crustal thickening is characterized by west-directed thick-skinned thrusting and development of a high-grade metamorphosed hinterland, which coincides with early thin-skinned thrusting and development of peak metamorphic conditions in the foreland. After the early compressional movement along the thrust system ended, deformation in the orogen transitioned into a transpressional phase, leading to the development of large sub-vertical shear zones overprinting previous flat-lying deformation fabrics and down-grading peak metamorphic assemblages (Battisti et al., 2018; De Toni, Bitencourt, Konopásek, et al., 2020; Percival et al., 2022).

Recent studies in the northern and central Dom Feliciano Belt have recognized the coupled tectono-metamorphic evolution of the orogenic foreland and hinterland domains. In the northern Dom Feliciano Belt (Santa Catarina state), low- to medium-grade metamorphism in the foreland records the progressive west-directed over-thrusting of the hinterland at c. 660–650 Ma, marking the earliest evidence of crustal thickening in the orogen (De Toni, Bitencourt, Konopásek, et al., 2020; Percival et al., 2022). The same relationship is inferred in the central sector of the belt (Rio Grande do Sul state) (Battisti et al., 2018; De Toni et al., 2021). In the southern Dom Feliciano Belt (Uruguay), west-directed thrusting and high temperature metamorphism at c. 650–640 Ma is documented only in the Punta del Este Terrane (Gross et al., 2009; Oyhantçabal et al., 2009), which is defined in this study as part of the orogenic hinterland. The evolution of the southern foreland, however, is more complex, and events are not as well understood, in part owing to strong reworking by post-collisional sub-vertical shear zones during the transpressional stage of orogenesis. Although there are abundant geochronological data from the hinterland and the

surrounding shear zones (Lenz et al., 2011; Masquelin et al., 2011; Oriolo et al., 2016, 2016; Oyhantçabal et al., 2009; Will et al., 2019), geochronological constraints for the Neoproterozoic metamorphic history of the foreland are lacking. As such, it is difficult to compare the evolutionary histories of the foreland and hinterland domains.

The aim of this work is to investigate the tectono-metamorphic evolution of the southern Dom Feliciano Belt foreland and hinterland domains in Uruguay, in particular the potential relationship between high-grade metamorphic units in both domains and the timing of crustal thickening and metamorphism in the foreland. Using detailed petrological and geochronological data, this work documents, and provides constraints on, the timing and conditions of two distinct tectonic events. Furthermore, the integration of this data with geochronological data from surrounding units is used to present a tectonic model for the evolution the southern Dom Feliciano Belt.

# 2 | GEOLOGICAL SETTING

The Dom Feliciano Belt is part of the larger Kaoko–Dom Feliciano–Gariép orogenic system, which forms the southernmost part of the SANOS (Figure 1b). The belt can broadly be divided into orogenic foreland and hinterland domains, which are generally further divided into a series of tectonostratigraphic units parallel to the structural trend of the orogen. From east to west, these are (1) a high-grade metamorphic basement of the hinterland (Cerro Olivo, Várzea do Capivarita, and Porto Belo complexes) with locally preserved syn-orogenic cover, (2) the Granite Belt, (3) the Schist Belt, (4) the foreland basins, and (5) the foreland basement (Basei et al., 2000; De Toni, Bitencourt, Nardi, et al., 2020; Gross et al., 2006; Martil et al., 2017; Oyhantçabal et al., 2009; Preciozzi et al., 1999).

A large, upright shear zone named the Sierra Ballena Shear Zone separates the foreland to the west from the hinterland to the east. The hinterland is largely represented by the Punta del Este Terrane, which is comprised of pre-orogenic basement complexes intruded by voluminous syn- to post-collisional granitoids of the Aiguá Batholith, and overlain by late-Neoproterozoic sedimentary successions including the Rocha, Sierra de Aguirre, and San Carlos formations. The basement is comprised of high temperature granulite facies orthogneisses, paragneisses, amphibolites, and migmatites of the Cerro Olivo Complex. Protolith ages from orthogneisses in this complex record an important magmatic episode during the middle Neoproterozoic at c. 800–770 Ma (Lenz et al., 2011; Masquelin et al., 2011; Oyhantçabal

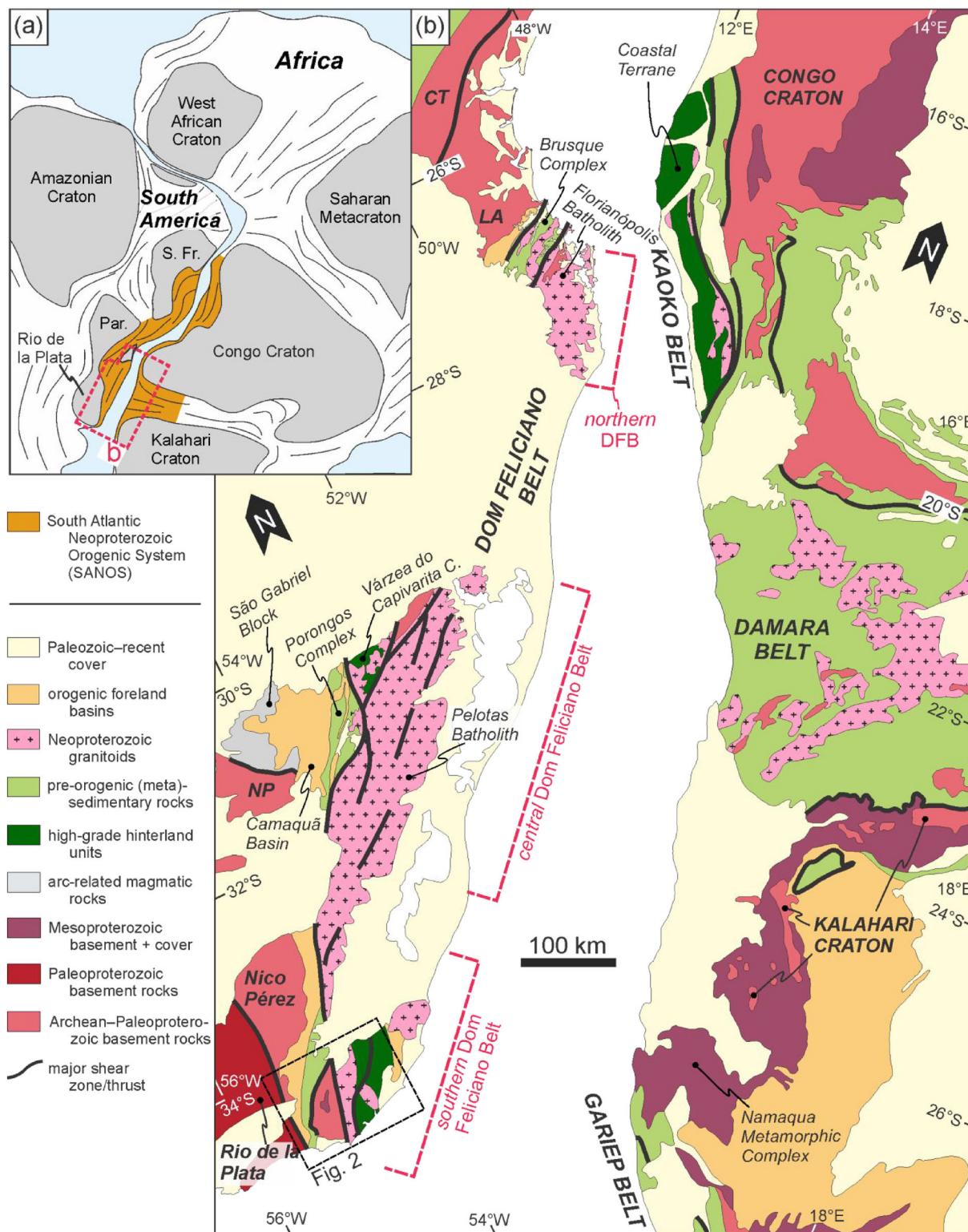


**FIGURE 1** (a) Schematic reconstruction of Western Gondwana showing the location of the SANOS (modified from Konopásek et al., 2020). S. Fr.—São Francisco Craton; Par.—Paranapanema Craton. (b) Simplified geological map of the southern SANOS (modified from Bitencourt & Nardi, 2000; De Toni et al., 2021; Konopásek et al., 2017; McCourt et al., 2013; Oyhançabal et al., 2011), showing the position of the African and south American continents at the onset of the opening of the South Atlantic Ocean (after Heine et al., 2013). LA—Luis Alves Craton.



et al., 2009). Similar ages are preserved in the Várzea do Capivarita and Porto Belo complexes in the central and northern Dom Feliciano Belt, respectively, and in the Coastal Terrane in the Kaoko Belt (Battisti et al., 2023; De Toni, Bitencourt, Nardi, et al., 2020; Konopásek et al., 2008; Martil, 2016). This magmatic event has been interpreted as recording pre-orogenic rifting, potentially linked to rifting of the Nico Pérez–Luis Alves Terrane from the Congo Craton during the breakup of Rodinia (Konopásek et al., 2018; Oriolo et al., 2016; Oyhançabal et al., 2009, 2018; Rapela et al., 2011; Will et al., 2019), or continental arc magmatism (De Toni, Bitencourt, Nardi, et al., 2020; Lenz et al., 2011, 2013; Masquelin et al., 2011). Central to the latter interpretation is the arc-like geochemical signature preserved in the rocks, although Konopásek et al. (2018) have argued that this may be inherited from crustal sources, and that the geochemical signature can be compatible with either a back-arc or purely continental rift-related setting.

To the west, the foreland consists of cratonic basement overlain by a series of Paleo- to Neoproterozoic supracrustal sequences (Figure 2a,b). The Nico Pérez Terrane represents the reworked cratonic margin of the belt, which is separated from the relatively unaffected Piedra Alta Terrane, part of the Rio de la Plata Craton, by the Sarandí del Yí Shear Zone along its western boundary (Oriolo et al., 2015; Rapela et al., 2011). The Nico Pérez Terrane is comprised of several Archean to Paleoproterozoic basement units that have been reworked during the Neoproterozoic (Masquelin et al., 2021; Oyhançabal et al., 2011, 2012). Recent works have highlighted the allochthonous nature of the Nico Pérez Terrane relative to the Rio de la Plata Craton (Oyhançabal et al., 2011; Rapela et al., 2011), and its likely origin as a part of the Congo Craton rifted away prior to orogenesis (Hueck et al., 2022; Oriolo et al., 2015, 2016; Oyhançabal et al., 2021; Percival et al., 2021).

The foreland basement is overlain by (now metamorphosed) pre-orogenic sedimentary sequences of the Schist Belt, known as the Lavalleya Complex (*sensu lato*), as well as Ediacaran syn- to post-collisional foreland basin deposits (Basei et al., 2000; Oyhançabal et al., 2021). Although the litho- and tectono-stratigraphy of the metasedimentary sequences is complex and poorly defined (see Oyhançabal et al., 2021), the strongly metamorphosed and deformed supracrustal rocks belonging to the Lavalleya Complex (Schist Belt) can generally be divided into two pre-Neoproterozoic units; the Cebollatí and Zanja del Tigre complexes (Hartmann et al., 2001; Oriolo et al., 2019; Oyhançabal et al., 2021). The potential correlation of the pre-orogenic sedimentary history of the Lavalleya Complex in Uruguay with the Schist Belt in the central and northern Dom Feliciano Belt is complicated

by the apparent predominance of Paleoproterozoic to Mesoproterozoic sedimentary ages (Chiglini et al., 2010; Gaucher et al., 2011; Hartmann et al., 2001; Oriolo et al., 2019; Oyhançabal et al., 2018). This contrasts with the Schist Belt in Brazil where early-Neoproterozoic (Tonian) sedimentary ages dominate (Percival et al., 2021; Pertille et al., 2017; Saalman et al., 2011). The metasedimentary rocks of the Schist Belt in Uruguay show a range in metamorphic grade from lower-greenschist to lower-amphibolite facies (Hartmann et al., 2001; Sánchez et al., 2001). Both the basement and supracrustal units are intruded by syn- to post-collisional granitoids ranging in age from c. 635 to 585 Ma (Lara et al., 2017; Oyhançabal et al., 2007, 2012).

The Campanero Unit represents a basement inlier of the Nico Pérez Terrane and consists of c. 1.7 Ga orthogneisses with subordinate high-temperature amphibolites and metasedimentary migmatites (Mallmann et al., 2007; Sánchez-Bettucci et al., 2004). From previous structural studies, the Campanero Unit is generally accepted to be a basement nappe that has been thrust over the Schist Belt (Mallmann et al., 2007; Oyhançabal et al., 2018; Rossini & Legrand, 2003). Although the timing of high-T metamorphism in the Campanero Unit is so far unknown, the final cooling below  $\sim 500^{\circ}\text{C}$  and potential exhumation of the unit, and thus the minimum age for metamorphism, is constrained by Ar–Ar in hornblende to c.  $564 \pm 4$  Ma (Oyhançabal et al., 2009).

The Zanja del Tigre Complex forms part of the Schist Belt outcropping immediately to the north and west of the Campanero Unit, and is comprised of a metamorphosed sedimentary sequence including metapelites, metapsammites, marbles, felsic metavolcanics, and gabbros (Oriolo et al., 2019). The metamorphic grade ranges from greenschist facies in the majority of the complex to lower-amphibolite facies conditions close to the contact with the Campanero Unit (Sánchez et al., 2001). U–Pb concordia ages from igneous zircon in metavolcanic and metagabbroic rocks within the complex constrain the timing of sedimentation to between c. 1480 and 1430 Ma (Gaucher et al., 2011; Oriolo et al., 2019).

### 3 | FIELD RELATIONSHIPS—DEFORMATION AND METAMORPHISM

The primary structural feature of the hinterland basement (Cerro Olivo Complex) is a high-temperature deformation fabric trending  $\sim 060^{\circ}$  (S1; Figure 2e). The fabric is characterized predominantly by granoblastic gneisses and granulites varying in structure from strongly banded (Figure 3a) to weakly foliated with large garnet porphyroblasts



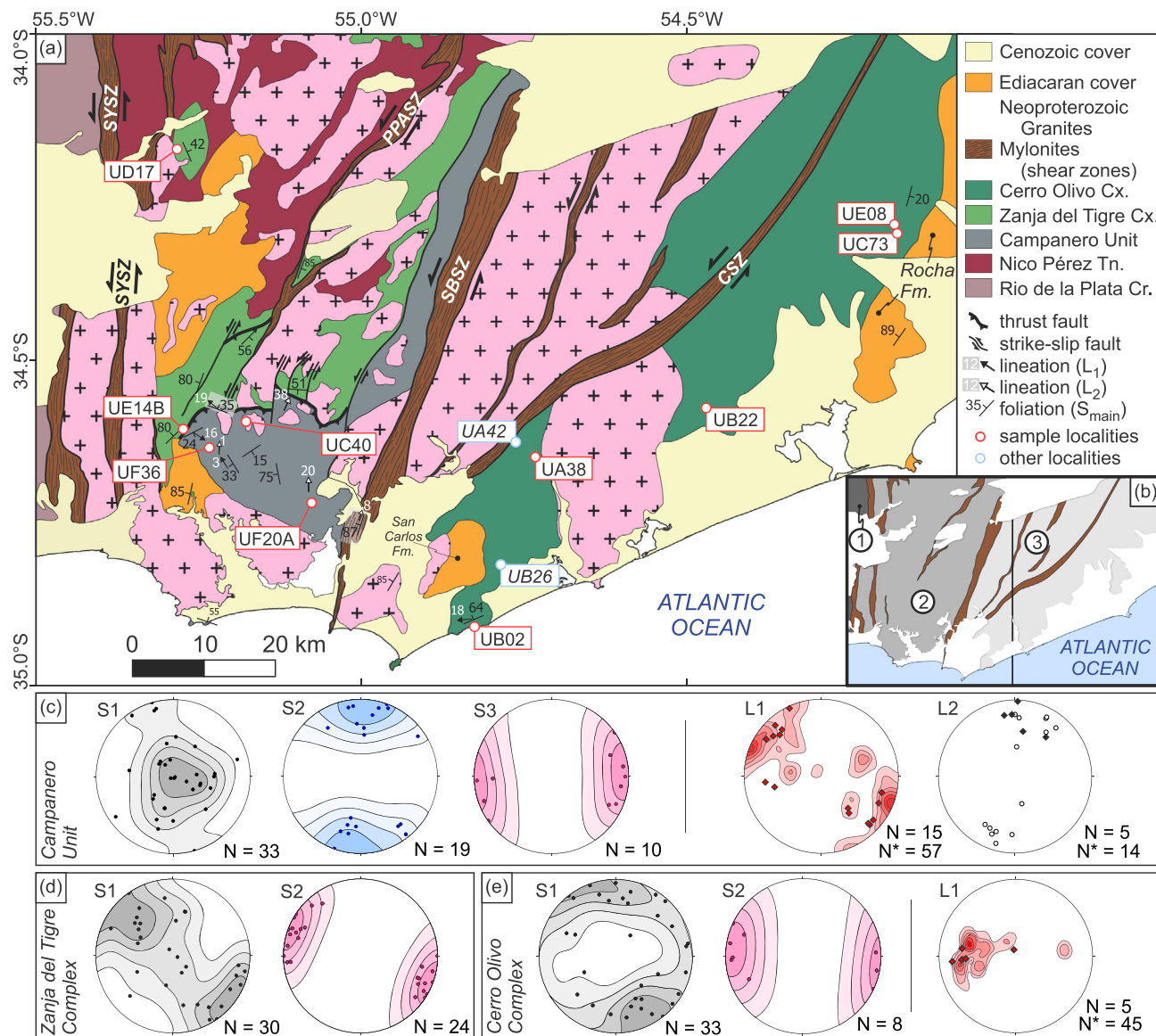


**FIGURE 2** (a) Simplified geological map of the Dom Feliciano Belt in Uruguay (modified and compiled from Oriolo et al. (2016); Oyhançabal et al. (2009); Spoturno et al. (2012); Spoturno et al. (2019)). Abbreviations for shear zones: SYSZ—Sarandi del Yí Shear Zone; PPASZ—Puntas del Pan de Azúcar Shear Zone; SBSZ—Sierra Ballena Shear Zone; CSZ—Cordillera Shear Zone. (b) Simplified tectonic map of the same area, showing 1—Rio de la Plata Craton, 2—Nico Pérez Terrane (foreland), and 3—Punta del Este Terrane (hinterland). Equal area lower hemisphere stereographic projections showing poles to plane and lineation structural data from selected units: (c) Campanero Unit (contours in L<sub>1</sub> and circles in L<sub>2</sub> from Oyhançabal et al. (2009), filled diamonds from this study); (d) Zanja del Tigre Complex; (e) Cerro Olivo Complex (contours in L<sub>1</sub> from Gross et al. (2009), filled diamonds from this study). N\* denotes the number of data from other datasets.

(Figure 3b). A stretching lineation (L<sub>1</sub>) associated with this high-T deformation trends predominantly E–W with shallow to moderate plunge (Figures 2e and 3a), and includes stretched quartz and feldspar aggregates and oriented metamorphic minerals such as sillimanite. Minor outcrops of deformed porphyritic granite contain large K-feldspar porphyroclasts stretched and oriented with the main lineation trend (Figure 3c). The L<sub>1</sub> lineation has been interpreted to indicate west-directed tectonic

transport during high-T metamorphism and foliation development (Masquelin et al., 2011). The complex is transected by the NE to NNE-trending, steeply dipping Cordillera Shear Zone (Figure 2a), which in some locations contains a sub-horizontal stretching lineation (L<sub>2</sub>) and evidence of sinistral shear sense (Masquelin et al., 2011; Oyhançabal et al., 2009).

The primary fabric in the Campanero Unit is a high-grade gneissic to mylonitic foliation (S<sub>1</sub>; Figures 2c and



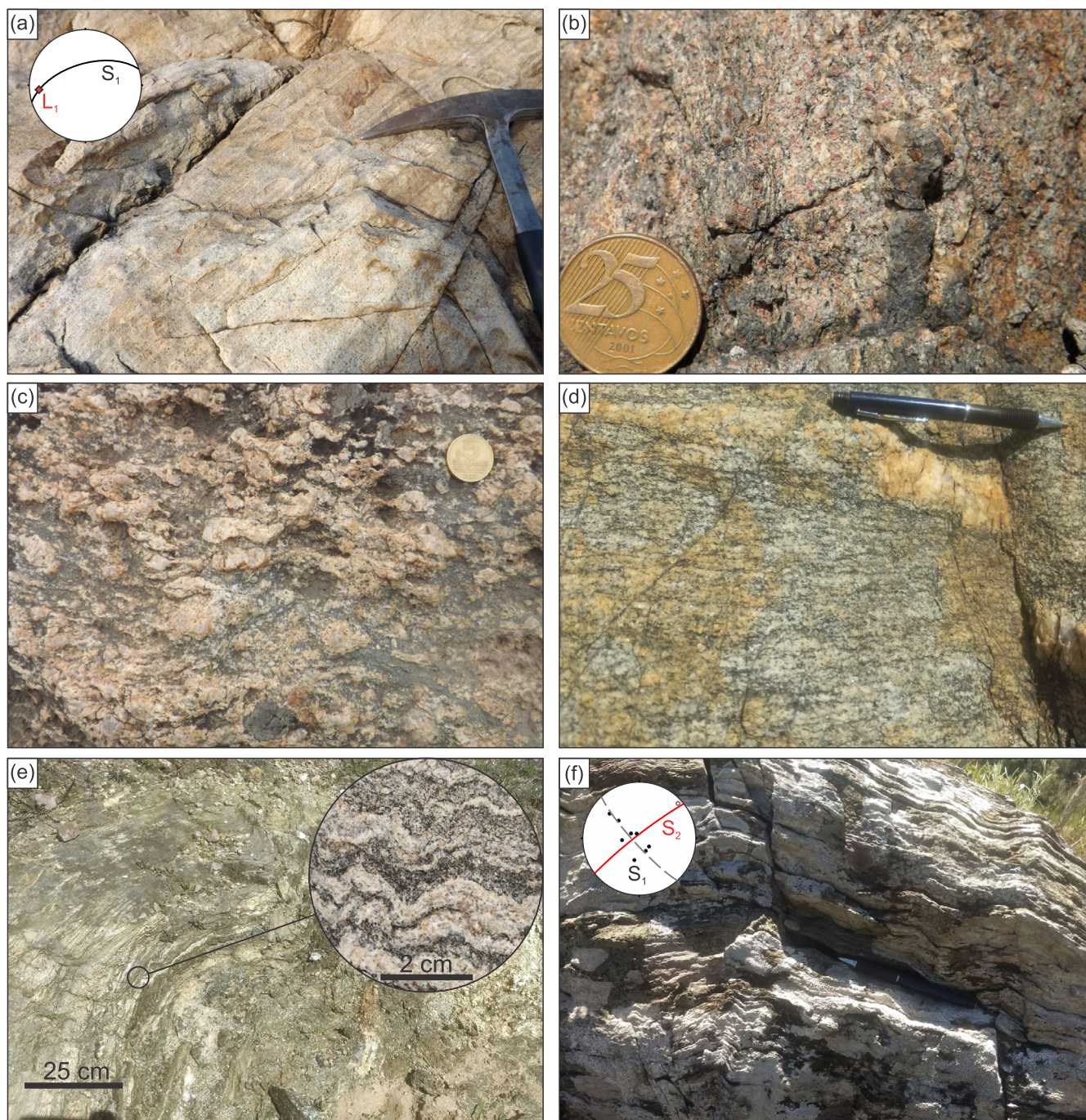


**FIGURE 3** Main outcrop-scale textural and structural features of the Campanero Unit, Zanja del Tigre Complex, and Cerro Olivo Complex. (a) Orthogneiss from the Campanero Unit showing  $S_1$  (S 34.90377°, W 55.23678°). (b) Melano-mesocratic part of gneiss from the Campanero Unit (S 34.59390°, W 55.17511°, locality UC40), with inset showing textural detail of sample UC4. (c) F2 folding and  $S_2$  crenulation cleavage in phyllite of the Zanja del Tigre Complex (E 34.58506°, W 55.15748°), with inset showing stereonet of poles to plane  $S_1$  data (black dots) fitting along a girdle (dashed line) describing F2 folding (fold axis marked by open circle) consistent with axial plane-parallel cleavage  $S_2$  (red line). (d) Strongly foliated grt-sil-gneiss from the Cerro Olivo Complex (S 34.90849°, W 54.82512°, locality UB02), with stereonet inset showing the orientation of  $S_1$  (black line) and  $L_1$  (red circle). (e) Weakly foliated gneiss from the Cerro Olivo Complex, showing coarse-grained texture and large garnet porphyroblasts (S 34.30564°, W 54.17755°, locality UC73). (f) Deformed porphyritic granite of the Cerro Olivo Complex (S 34.64827°, W 54.73200°, locality UA38), showing stretched K-feldspar porphyroblasts.



3d,e). This predominantly flat-lying fabric is overprinted by two mutually near-orthogonal foliations, S2 and S3 (Figure 2c), and associated macro-scale folding. Foliation S2 trends E–W and is defined by parallel muscovite and biotite overprinting the high-T S1 gneissic fabric. Foliation S3 is oriented N–S, largely parallel with the Sierra Ballena Shear Zone and thus comparable to S2 in the other units (Figure 2c–e). The two overprinting foliations (S2 and S3) show similar metamorphic grade and degree of deformation and based on field observations it is difficult to unequivocally determine their relative age.

Two near-orthogonal stretching lineations are observed in the Campanero Unit; one trending NW–SE (L1) and another trending NNE–SSW (L2) (Figure 2c). Due to similarities in orientation, the L1 stretching lineation in the Campanero Unit has been correlated with L1 in the Cerro Olivo Complex (Oyhantçabal et al., 2009), and thus potentially records early west-directed tangential shearing. Lineation L1 appears to be folded towards parallelism with the Sierra Ballena Shear Zone (see Oyhantçabal et al., 2009), suggesting it has been deformed by, and thus predates, sinistral shearing along this boundary. Lineation L2, on the other hand, lies parallel to the Sierra Ballena Shear Zone suggesting that it developed during the later sinistral transpressional event. L2 is contained predominantly within the N–S-trending S3 foliation and associated small shear zones, although some outcrops show lineations with similar orientation within the E–W-trending S2 foliation. Considering this, and the potential partitioning of strain within, and adjacent to, the Campanero Unit, it is possible that the development of S2 and S3 was largely contemporaneous.

The dominant fabric in the Zanja del Tigre Complex is a low-grade schistosity (S1; Figures 2d and 3f) characterized by lepidoblastic muscovite  $\pm$  chlorite  $\pm$  biotite. Foliation S1 is deformed by F2 folds with axes largely parallel to the Sierra Ballena Shear Zone, and is overprinted by an often pervasive axial planar crenulation cleavage (S2; Figures 2d and 3f). Sánchez et al. (2001) described the same structural features across the whole of the southern part of the Schist Belt in Uruguay, and observed ubiquitous NW-directed thrust faults transecting the supracrustal rocks that are likely contemporaneous with the development of F2 and S2. Sánchez et al. (2001) further reported that the metamorphic grade in the Schist Belt increases from lower-greenschist facies to lower-amphibolite facies towards the southeast and the contact with the Campanero Unit, where the presence of staurolite and garnet marks the highest-grade rocks in this region. However, rocks showing lower-amphibolite-facies metamorphic conditions can also be found in the west of the Zanja del Tigre Complex (locality UD17;

Figure 2a), as well as in the northeast within the Cebollati Complex (Hartmann et al., 2001).

## 4 | SAMPLE DESCRIPTION AND MINERAL CHEMISTRY

Five samples from the Cerro Olivo Complex, two from the Campanero Unit, and two from the Schist Belt were collected for thermodynamic modelling and/or geochronological analysis (Figure 2a). Of the samples used for thermodynamic modelling, mineral major element compositions were analysed using an electron microprobe CAMECA SX100 at the Faculty of Natural Sciences, Masaryk University in Brno, Czech Republic. Representative analyses are given in Supporting Information Tables S1–S3, and detailed analytical methods are given in Supporting Information Text S1. Mineral abbreviations follow Whitney and Evans (2010). Mineral compositions and endmember proportions are reported as follows:  $X_{Mg} = Mg/(Mg + Fe)$ ,  $X_{Sps} = Mn/(Mn + Fe + Mg + Ca)$ ,  $X_{Alm} = Fe/(Mn + Fe + Mg + Ca)$ ,  $X_{Prp} = Mg/(Mn + Fe + Mg + Ca)$ ,  $X_{Grs} = Ca/(Mn + Fe + Mg + Ca)$ ,  $X_{An} = Ca/(Ca + Na + K)$ .

### 4.1 | Samples from the Cerro Olivo complex

Sample UB02 (S 34.90849°, W 54.82512°) is a fine-grained felsic gneiss collected from the Cerro Olivo Complex. Macroscopically, the rock shows a gneissic fabric (Figure 3a) and contains the mineral assemblage Qz–Pl–Kfs–Grt–Bt–Sil, with minor ilmenite and rutile. Under the microscope the fabric is indistinct and the rock matrix is dominated by quartz and feldspar (plagioclase:  $X_{An} = 0.35–0.36$ ), showing granoblastic texture with discontinuous ribbons of K-feldspar marked by low concentrations of ilmenite that likely represent recrystallized phenocrysts (Figure 4a). Otherwise, all the mineral phases appear to be homogeneously distributed within the rock. Sillimanite grains are partially retrogressed and surrounded by sericite halos (Figure 4a). Garnet grains are small (<250  $\mu m$ ) and rounded to irregular in shape (Figure 4b), and there is only minor compositional variation in garnet from core to rim (core:  $Sps_{0.02}Alm_{0.73}Prp_{0.22}Grs_{0.03}$  – rim:  $Sps_{0.01}Alm_{0.70}Prp_{0.26}Grs_{0.03}$ ; Figure 5a), suggesting diffusional resetting. Biotite grains ( $X_{Mg} = 0.57–0.66$ ,  $Ti = 0.17–0.31$  a.p.f.u) are small (<250  $\mu m$ ) and uncommon.

Sample UB22 (S 34.57308°, W 54.470232°) is a medium-grained, grt-crd-gneiss collected from the Cerro Olivo Complex. The sample contains the mineral assemblage Qz–Pl–Kfs–Grt–Bt–Crd–Ilm. Compositional



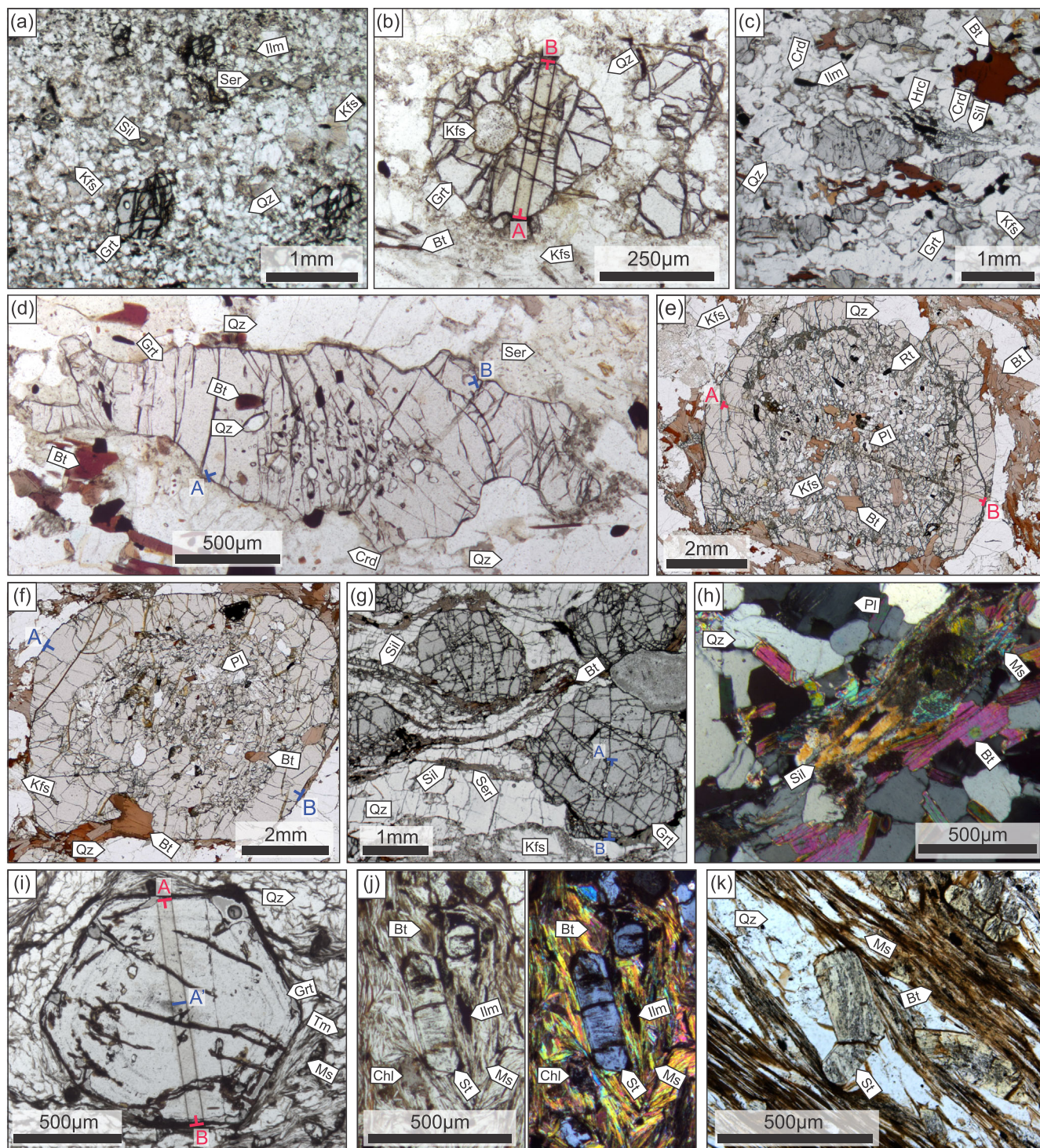
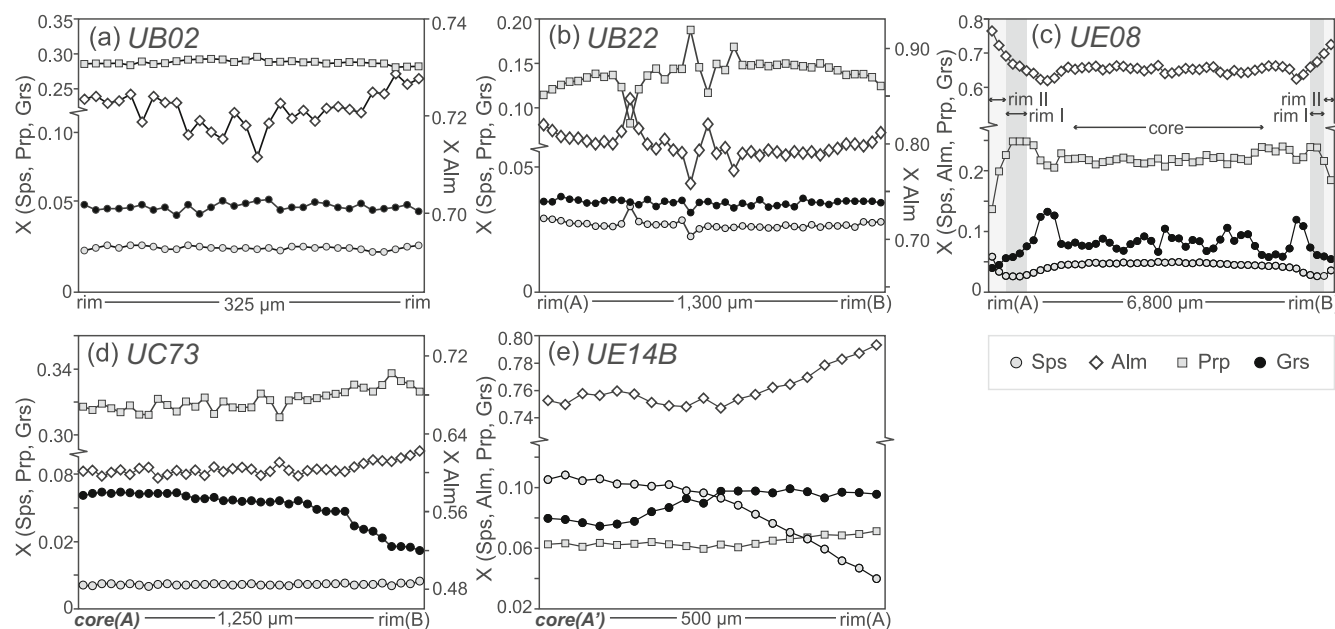


FIGURE 4 Legend on next page.



**FIGURE 4** Photomicrographs of thin sections showing representative mineral assemblages and textures from samples in this study. (a) Overview of fine-grained, granoblastic texture in grt-sill-gneiss (UB02) with Kfs ribbons marked by low-Ilm concentration defining the gneissic foliation, and Sill partially replaced by sericite; (b) analysed garnet from the same sample (UB02; line A–B shows transect from Figure 11e); (c) overview of coarse-grained gneissic texture in grt-crd-gneiss (UB22) showing alternating layers of Qz + Kfs and Crd enclosing Sill + Hrc + Ilm; (d) analysed garnet in the same sample (UB22) showing elongate, irregular shape with embayments of Crd, Qz and Kfs (Ser) (line A–B shows transect from Figure 5c); (e) large garnet porphyroblast in grt-bt-sill-gneiss (UE08) showing Bt and Rt inclusions (line A–B shows transect from Figure 11f) with typical coarse-grained matrix of Bt, Kfs, Qz and Pl; (f) large, rounded garnet from the same sample (UE08) showing abundant inclusions of Qz, Bt, Rt, and Fsp in the core, and a relatively inclusion-free rim (line A–B shows transect from Figure 5d); (g) overview of coarse-grained gneissic texture in grt-sill-bt-gneiss (UC73), with large, rounded to irregular garnets within quartzofeldspathic layers, and sill partially replaced by Ser (line A–B shows transect from Figure 5e); (h) Ms replacing sill in predominantly quartzofeldspathic matrix from bt-sill-gneiss (UC40); (i) euhedral garnet in grt-st-schist (UE14B) showing concentric micro-inclusions (line A–A' shows transect from Figure 5a; line A–B shows transect from Figure 11d); (j) St in Ms + Bt matrix from the same sample (UE14B) showing inclusion trails orthogonal to foliation; St in Qz + Bt + Ms matrix in grt-st-schist (UD17) containing larger Qz + oxide inclusions.



**FIGURE 5** Compositional profiles of garnet from samples used for phase equilibria modelling: (a) grt-sill-gneiss UB02; (b) grt-crd-gneiss UB22; (c) grt-bt-sill-gneiss UE08 (showing location of zones core, rim I and rim II); (d) grt-sill-bt-gneiss UC73; (e) grt-st-schist UE14B. Note that profiles (d) and (e) are from core to rim, while the rest are rim to rim.

sub-domains of cordierite ( $X_{Mg} = 0.49$ ) enclosing sillimanite, hercynite and ilmenite are also common (Figure 4c), suggesting that matrix sillimanite in the rocks could have been completely exhausted during the cordierite-forming reaction. Secondary sericite is often found replacing feldspar (Figure 4d). Garnet porphyroblasts have irregular shapes with common embayments of quartz and feldspar/sericite, and reach up to c. 1.5 mm in width (Figure 4c,d). Garnet is Alm-rich and grains do not vary much in composition from core to rim (core:  $Sps_{0.03}Alm_{0.82}Prp_{0.11}Grs_{0.04}$  – rim:  $Sps_{0.03}Alm_{0.79}Prp_{0.15}Grs_{0.04}$ ; Figure 5b), suggesting diffusional resetting. The cores of garnet porphyroblasts contain <100 µm rounded inclusions of quartz, biotite

( $X_{Mg} = 0.44$ ,  $Ti = 0.31$  a.p.f.u.), ilmenite and hercynite. A weak gneissic foliation is defined by alternating cordierite-rich and quartz-feldspar-rich (plagioclase:  $X_{An} = 0.36$ – $0.42$ ) bands. Matrix biotite ( $X_{Mg} = 0.39$ – $0.40$ ,  $Ti = 0.18$ – $0.20$  a.p.f.u.) and elongated garnet grains are oriented parallel with this fabric.

Sample UE08 (S 34.29184°, W 54.18184°) is a coarse-grained gneiss collected from the Cerro Olivo Complex. The sample contains the mineral assemblage Qz–Pl–Kfs–Bt–Grt–Sil, with accessory ilmenite and rutile, and secondary muscovite. Garnet porphyroblasts are large, reaching up to 7 mm in diameter, and the largest grains contain abundant inclusions of rounded biotite ( $X_{Mg} = 0.58$ – $0.59$ ;  $Ti = 0.25$ – $0.27$  a.p.f.u.), plagioclase

( $X_{\text{An}} = 0.42\text{--}0.46$ ), quartz, rutile and ilmenite (Figure 4e, f). No rutile is found in the matrix. Garnet is Alm-rich and shows three compositional zones: core, rim I, and rim II. The compositional profile from the core through to rim I is consistent with prograde growth (average core:  $\text{Sps}_{0.05}\text{Alm}_{0.65}\text{Prp}_{0.22}\text{Grs}_{0.08}$  – average rim I:  $\text{Sps}_{0.03}\text{Alm}_{0.67}\text{Prp}_{0.24}\text{Grs}_{0.06}$ ; Figure 5c), which is followed by a distinct change in chemistry at rim II (average rim II:  $\text{Sps}_{0.05}\text{Alm}_{0.71}\text{Prp}_{0.20}\text{Grs}_{0.03}$ ; Figure 5c) with a spike in Sps content suggesting possible resorption. Matrix biotite ( $X_{\text{Mg}} = 0.44\text{--}0.46$ ,  $\text{Ti} = 0.28\text{--}0.31$  a.p.f.u.) is randomly oriented and predominantly located interstitially between larger matrix plagioclase ( $X_{\text{An}} = 0.31\text{--}0.38$ ), quartz, and garnet grains, and occasionally clearly replacing embayed garnet rims (Figure 4f). All the mineral phases appear to be regularly distributed throughout the examined thin sections and no compositional sub-domains were observed.

Sample UC73 (S 34.30564°, W 54.17755°) is a coarse-grained felsic gneiss collected from the Cerro Olivo Complex. The sample shows a gneissic foliation defined by alternating quartz-rich and feldspar-rich layers (Figure 4g) and contains the mineral assemblage Qz–Pl–Kfs–Bt–Grt–Sil–Ilm. Garnet porphyroblasts are irregularly shaped with rounded edges, reaching up to 3 mm in diameter (Figure 4g). Most garnet grains contain cores with small (<20  $\mu\text{m}$ ), rounded inclusions of quartz, rutile, and biotite ( $X_{\text{Mg}} = 0.67$ ,  $\text{Ti} = 0.38$  a.p.f.u.), and a small number contain elongate ilmenite inclusions. There is no rutile in the matrix. Garnet is an Alm- and Prp-rich solid solution (Figure 5d) showing a slight increase in Sps content from core to rim (core:  $\text{Sps}_{0.01}\text{Alm}_{0.61}\text{Prp}_{0.31}\text{Grs}_{0.06}$  – rim:  $\text{Sps}_{0.02}\text{Alm}_{0.72}\text{Prp}_{0.22}\text{Grs}_{0.04}$  [Grt<sub>2</sub>, see Table S1]), suggesting diffusional resetting, and varying intensity of Alm and Prp zonation (see comparison in Table S1) which may be due to sectioning bias. Matrix biotite ( $X_{\text{Mg}} = 0.49\text{--}0.60$ ) is oriented parallel to the primary foliation, and is found interstitially between matrix plagioclase ( $X_{\text{An}} = 0.35$ ) and occasionally replacing garnet rims (Figure 4g), consistent with growth during a retrograde reaction involving hydrous melt (e.g., see Holness et al., 2011).

Sample UA38 (S 34.64827°, W 54.73200°) is a deformed porphyritic granite from the Cerro Olivo Complex. Large porphyroclasts of K-feldspar (up to several cm; Figure 3c) are surrounded by a recrystallized matrix of quartz, plagioclase, K-feldspar, biotite, and an opaque mineral, with accessory apatite and zircon. The coarse-grained nature of recrystallized feldspars and quartz points at high-temperature deformation, likely coeval with the formation of surrounding migmatites. Biotite is occasionally converted to chlorite, suggesting minor retrogression of the high-temperature mineral assemblage.

## 4.2 | Samples from the Campanero Unit

Sample UF36 (S 34.63407°, W 55.23149°) is an orthogneiss collected from the Campanero Unit. The sample contains the mineral assemblage Qz–Bt–Pl–Kfs, with accessory monazite and zircon. The rock is coarse-grained (c. 500  $\mu\text{m}$ ) and equigranular, pointing to deformation at high temperatures. Monazite grains are large, reaching up to c. 200  $\mu\text{m}$ . Shape preferred orientation of lepidoblastic biotite crystals define the primary (S1) foliation.

Sample UC40 (S 34.59390°, W 55.17511°) is a well-foliated, metasedimentary gneiss collected from the Campanero Unit. The rock consists of melanocratic–mesocratic banded gneisses (Figure 3e), occasionally interleaved with larger leucocratic layers. The former unit is coarse-grained, and contains the mineral assemblage Qz–Bt–Sil–Pl–Kfs with accessory monazite and zircon, and secondary muscovite (Figure 4h), and shows alternating light–dark gneissic banding between 1 and 5 cm thick, roughly in equal proportion, comprising biotite-rich ( $X_{\text{Mg}} = 0.66\text{--}0.68$ ,  $\text{Ti} = 0.08\text{--}0.09$  a.p.f.u.) and quartz–K-feldspar–plagioclase-rich ( $X_{\text{An}} = 0.15$ ) domains. The leucocratic parts are predominantly quartz–feldspathic with small amounts of biotite and accessory zircon. Due to the extent of deformation it is not clear from field relationships whether the leucocratic parts represent leucosomes or felsic dykes that intruded the (meta)sedimentary protolith of the rock.

## 4.3 | Samples from the Schist Belt

Sample UE14B (S 34.60547°, W 55.27147°) is a metapelitic schist collected from the Zanja del Tigre Complex. The rock contains the mineral assemblage Qz–Ms–Bt–Grt–St–Ilm, with secondary chlorite. Garnet grains are euhedral crystals up to 1 mm across (Figure 4i), and show chemical zoning with decreasing Sps, and increasing Alm, Prp and Grs components from core to rim (core:  $\text{Sps}_{0.10}\text{Alm}_{0.75}\text{Prp}_{0.06}\text{Grs}_{0.08}$  – rim:  $\text{Sps}_{0.04}\text{Alm}_{0.79}\text{Prp}_{0.07}\text{Grs}_{0.10}$ ; Figure 5e) interpreted as reflecting prograde growth. Garnet porphyroblasts show concentric zoning delineated by micro inclusions of opaque oxides with no evidence of preferred orientation, suggesting growth prior to the development of a strong foliation (Figure 4i). Staurolite grains ( $X_{\text{Mg}} = 0.10\text{--}0.14$ ), in contrast, contain more abundant inclusions of opaque oxides and quartz, oriented orthogonal to the primary fabric and the long axis of the staurolite grains (Figure 4j) suggesting syn- to post-kinematic growth. Biotite ( $X_{\text{Mg}} = 0.36\text{--}0.38$ ,  $\text{Ti} = 0.06\text{--}0.09$  a.p.f.u.) is commonly overgrown by S2-parallel muscovite, and very



occasionally replaced by secondary chlorite. The dominant fabric is a strong crenulation cleavage oriented 035/70E, likely transposing S1 and apparently coeval with the peak metamorphic assemblage at this locality.

Sample UD17 (S 34.17881°, W 55.28727°) is a metapelitic schist collected from the north-western Schist Belt, close to the contact with the Sarandí del Yí Shear Zone (Figure 2a). The rock contains the same mineral assemblage as sample UE14B (Qz–Ms–Bt–Grt–St–Ilm). Euhe-dral garnet grains (~1 mm) also show chemical growth zoning with decreasing Sps and Grs and increasing Alm and Prp component from core to rim (core: Sps<sub>0.11</sub>Alm<sub>0.73</sub>Prp<sub>0.06</sub>Grs<sub>0.1</sub> – rim: Sps<sub>0.07</sub>Alm<sub>0.80</sub>Prp<sub>0.07</sub>Grs<sub>0.06</sub>), which we interpret as reflecting prograde growth. Staurolite ( $X_{Mg} = 0.09$ – $0.11$ ) and biotite ( $X_{Mg} = 0.35$ ; Ti = 0.09–0.10 a.p.f.u.) grains show similar size, shape, and composition to those in sample UE14B, and staurolite similarly contains oriented inclusions of quartz and ilmenite (Figure 4k).

## 5 | PHASE EQUILIBRIA MODELLING

P–T estimates were calculated using the PerpleX software package of Connolly (2005) (ver. 6.9.0) with the thermodynamic data set DS6.22 of Holland and Powell (2011). The following solution models were used for all pseudosections: garnet, chlorite, chloritoid, cordierite, white mica, biotite, and staurolite from White et al. (2014), ternary feldspar from Fuhrman and Lindsley (1988), and ilmenite from White et al. (2000) as modified by White et al. (2014). In addition, the melt model from White et al. (2014) was used to calculate pseudosections for the high temperature samples (UE08, UB02, UB22, UC73, and UC40), and the spinel model from White et al. (2002) was used for sample UB22.

All pseudosections were modelled in the MnO–Na<sub>2</sub>O–CaO–K<sub>2</sub>O–FeO–MgO–Al<sub>2</sub>O<sub>3</sub>–SiO<sub>2</sub>–H<sub>2</sub>O–TiO<sub>2</sub> (MnNCKFMASHT) system. Bulk rock compositions used for calculations were estimated from whole-rock powder analysis conducted by lithium borate fusion inductively coupled plasma emission spectroscopy (ICP ES) at Bureau Veritas Mineral Laboratories in Vancouver, Canada, and are presented with the pseudosection figures. None of the analysed samples contain minerals with a significant Fe<sub>2</sub>O<sub>3</sub> component, so the system was simplified by excluding O<sub>2</sub>/Fe<sub>2</sub>O<sub>3</sub>. Samples that show evidence of supra-solidus metamorphic equilibration (based on exploratory pseudosection models) were modelled using constrained H<sub>2</sub>O so as to model melt-present phase fields. H<sub>2</sub>O concentration was estimated using the bulk sample loss-on-ignition. Samples UE14B and UD17, which are

both sub-solidus metapelites, were modelled in H<sub>2</sub>O-saturated conditions, assuming free H<sub>2</sub>O. Mineral compositional contours were calculated for each pseudosection and compared with the observed values as determined by microprobe analysis to better constrain the estimated P–T conditions (e.g., Stüwe & Powell, 1995). Table S4 presents the modelled PT conditions for each sample together with a comparison of the observed vs. modelled mineral compositional parameters based on mean PT values as a way to demonstrate the goodness of the intersection of compositional contours.

Prograde metamorphic garnet growth up to upper amphibolite facies has been shown to fractionate elements faster than diffusional processes can maintain equilibrium, resulting in the progressive removal of elements from metamorphic reactions in the rock matrix (Caddick et al., 2010; Marmo et al., 2002). Using the  $X_{Sps}$  component as an indicator of Rayleigh fractionation during prograde growth (Hollister, 1966), only garnet from samples UE14B, UD17, and UE08 show evidence of typical prograde growth without significant diffusional re-equilibration (Figure 5). For this reason, garnet fractionation calculations were conducted for these samples to better constrain peak metamorphic conditions. For the other samples, garnet core compositions have mostly been ignored as they show evidence of significant diffusion, and so cannot reliably give information about early prograde garnet growth.

Granulites commonly reflect the residuum product of melting processes. As such, partial melt extraction from granulite facies rocks has the potential to fractionate elements from their protolith compositions, potentially obfuscating estimates of P–T conditions for garnet core growth and early prograde metamorphic histories (Bartoli, 2017; Indares et al., 2008; White et al., 2004). Melt-reintegration calculations can be used to investigate these early prograde histories. Although there is no strong evidence for relict melt in the Cerro Olivo Complex samples, the high-T metamorphic conditions recorded in the rocks suggests that partial melting may have resulted in significant melt loss. Of the granulite facies samples in this study, however, only garnet cores from sample UE08 show evidence of relict prograde growth, so inferring a P–T path for melt reintegration is difficult or ineffective for the remaining samples. Melt reintegration calculations for sample UE08 (data not shown), following the single-step method of Indares et al. (2008), indicate that the rock underwent only minor melt loss (<5 wt%), and models calculated using the resulting (pre-melt loss) protolith bulk composition do not show significantly different mineral compositional isopleths or shapes of relevant stability fields when compared to calculations using the measured bulk composition. Because

of this, we present models for sample UE08 using garnet-fractionated and unfractionated bulk compositions under the assumption that the measured bulk composition is an accurate reflection of the rock's reactive composition during its metamorphic evolution.

## 5.1 | Modelling samples from the Cerro Olivo Complex

Figure 6a shows a pseudosection calculated in  $H_2O$ -undersaturated conditions for sample UB02, and is contoured for  $X_{Sps}$ ,  $X_{Alm}$ ,  $X_{Prp}$ , and  $X_{Grs}$  content in garnet (Figure 6b,c), Ti (a.p.f.u.) in biotite (Figure 6d), and  $X_{An}$  in plagioclase (Figure 6e). The compositional isopleths for garnet rims ( $Sps_{0.01}Alm_{0.70}Prp_{0.26}Grs_{0.03}$ ), biotite ( $Ti = 0.17$ – $0.31$  a.p.f.u.), and plagioclase ( $X_{An} = 0.35$ – $0.36$ ) intersect within the phase field containing the observed mineral assemblage Bt–Grt–Pl–Kfs–Sil–Ilm–melt, suggesting that the matrix equilibrated at 5.2–7.2 kbar and 780–800°C (circled in Figure 6a–e).

Figure 6f shows a pseudosection calculated for sample UB22 in  $H_2O$ -undersaturated conditions, and is contoured for observed  $X_{Sps}$ ,  $X_{Alm}$ ,  $X_{Prp}$ , and  $X_{Grs}$  in garnet (Figure 6g,h),  $X_{Mg}$  in cordierite, Ti (a.p.f.u.) in biotite (Figure 6i) and  $X_{An}$  in plagioclase (Figure 6j). The compositional isopleths for garnet rims ( $Sps_{0.03}Alm_{0.79}Prp_{0.15}Grs_{0.04}$ ), biotite ( $Ti = 0.18$ – $0.20$  a.p.f.u.), cordierite ( $X_{Mg} = 0.49$ ) and plagioclase ( $X_{An} = 0.36$ – $0.42$ ) intersect within the phase fields containing the observed dominant assemblage of Bt–Grt–Pl–Kfs–Crd–Ilm–melt  $\pm$  Sil, constraining matrix metamorphic equilibration conditions to 4.0–4.5 kbar and 745–755°C (circled in Figure 6f–j). The pseudosection suggests the growth of cordierite at the expense of sillimanite (and likely biotite or melt, depending on the direction of the PT path), which shows good agreement with microtextural observations. This suggests that the ribbons of cordierite may be related to a retrograde reaction involving hydrous melt, explaining the absence of obvious melt textures. Furthermore, the reaction as shown in the model suggests that matrix equilibration textures are the result of decompression from higher pressures.

Figure 7a shows a pseudosection calculated for sample UE08 in  $H_2O$ -undersaturated conditions using the measured bulk rock composition. Contoured isopleths are calculated for  $X_{Sps}$ ,  $X_{Alm}$ ,  $X_{Prp}$ , and  $X_{Grs}$  content in garnet cores (Figure 7b,c), and for  $X_{Mg}$  in biotite and  $X_{An}$  in plagioclase inclusions within garnet (Figure 7d). Compositional isopleths for garnet cores ( $Sps_{0.05}Alm_{0.65}Prp_{0.22}Grs_{0.08}$ ) and biotite inclusions within garnet ( $X_{Mg} = 0.58$ – $0.59$ ) intersect within an error of 0.01 at 9.7–11.4 kbar and 760–780°C (circled in

Figure 7a–c). Compositional isopleths for  $X_{Sps}$ ,  $X_{Alm}$ , and  $X_{Grs}$  content in garnet rim II ( $Sps_{0.05}Alm_{0.71}Prp_{0.20}Grs_{0.03}$ ),  $X_{Mg}$  in matrix biotite ( $X_{Mg} = 0.44$ – $0.46$ ), and  $X_{An}$  in matrix plagioclase ( $X_{An} = 0.31$ – $0.38$ ) intersect within the phase field containing the assemblage Bt–Grt–Pl–Kfs–Sil–Rt–melt, constraining matrix equilibration conditions to 6.5–9.2 kbar and 740–790°C (Figure 7c). Figure 7d shows a pseudosection calculated using a garnet-fractionated bulk composition calculated by fractionating garnet up to the P–T conditions estimated from the model presented in Figure 7a using the in-built PerpleX fractionation routine. Compositional isopleths for garnet rim I constrain the growth of this stage of garnet to 9.0–10.8 kbar and 770–800°C (circled in Figure 7e–g). The isopleths for rim II do not intersect in the fractionated model. The similarity in P–T estimates for the core and rim I indicates that the garnet does not preserve prograde growth, despite superficially prograde-like major element profiles, suggesting that garnet cores were likely significantly affected by diffusion during high-temperature metamorphism. Garnet rim II, in contrast, records later, lower-pressure re-equilibration and resorption of garnet, and the return of the bulk reactive composition to something more closely resembling the measured bulk.

Figure 8a shows a pseudosection calculated in  $H_2O$ -undersaturated conditions for sample UC73, which is contoured for  $X_{Sps}$ ,  $X_{Alm}$ ,  $X_{Prp}$ , and  $X_{Grs}$  in garnet (Figure 8b,c), and for  $X_{An}$  in plagioclase and  $X_{Mg}$  in biotite (Figure 8d,e). The isopleths for garnet cores ( $Sps_{0.01}Alm_{0.61}Prp_{0.31}Grs_{0.06}$ ) and biotite inclusions in garnet ( $X_{Mg} = 0.67$ ) are vertical and parallel with no pressure constraints, suggesting temperatures between 810 and 840°C. Rutile inclusions within garnet, however, suggest equilibration for garnet cores above  $\sim 7$  kbar. Compositional isopleths for garnet rims ( $Sps_{0.02}Alm_{0.72}Prp_{0.22}Grs_{0.04}$ ), matrix plagioclase ( $X_{An} = 0.35$ ), and matrix biotite rims ( $X_{Mg} = 0.49$ ) intersect within a phase field containing the observed assemblage Bt–Grt–Pl–Kfs–Sil–Ilm–melt, indicating matrix equilibration at 5.2–6.9 kbar and 775–790°C (circled in Figure 8a–e).

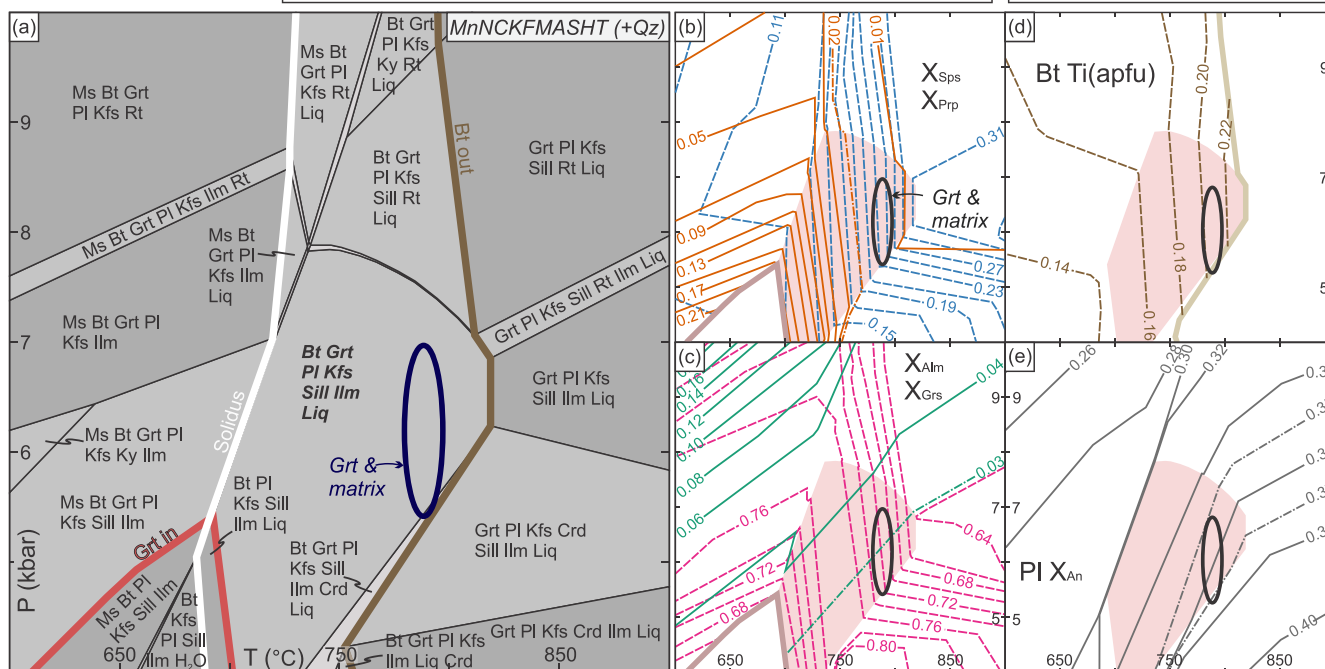
## 5.2 | Modelling the sample from the Campanero Unit

Figure 9 shows a pseudosection calculated in  $H_2O$ -undersaturated conditions for sample UC40 (Figure 9a), which is contoured for  $X_{Mg}$  and Ti (a.p.f.u.) in biotite (Figure 9b), and  $X_{An}$  in plagioclase (Figure 9c). The major element bulk composition was analysed from a sample of the mesocratic, biotite-rich part of the outcrop (see inset in Figure 3f), without any of the larger, cross-cutting leucocratic veins. There is no garnet in the sample to help

UB02 grt-sill-gneiss  
(without grt fractionation)

SiO <sub>2</sub> = 74.03	FeO = 2.23	CaO = 0.97	K <sub>2</sub> O = 5.45	MnO = 0.03
Al <sub>2</sub> O <sub>3</sub> = 13.51	MgO = 0.57	Na <sub>2</sub> O = 1.69	TiO <sub>2</sub> = 0.30	H <sub>2</sub> O = 0.70

--- Grt X <sub>Alm</sub>	--- Grt X <sub>Sps</sub>	--- Pl X <sub>An</sub>
--- Grt X <sub>Prp</sub>	--- Grt X <sub>Grs</sub>	--- Bt Ti(apfu)

UB22 grt-crd-gneiss  
(without grt fractionation)

SiO <sub>2</sub> = 61.70	FeO = 11.03	CaO = 0.45	K <sub>2</sub> O = 2.20	MnO = 0.25
Al <sub>2</sub> O <sub>3</sub> = 16.91	MgO = 2.61	Na <sub>2</sub> O = 0.56	TiO <sub>2</sub> = 1.66	H <sub>2</sub> O = 1.10

--- Grt X <sub>Sps</sub>	--- Grt X <sub>Alm</sub>	--- Pl X <sub>An</sub>	--- Crd X <sub>Mg</sub>
--- Grt X <sub>Grs</sub>	--- Grt X <sub>Prp</sub>	--- Bt Ti(apfu)	

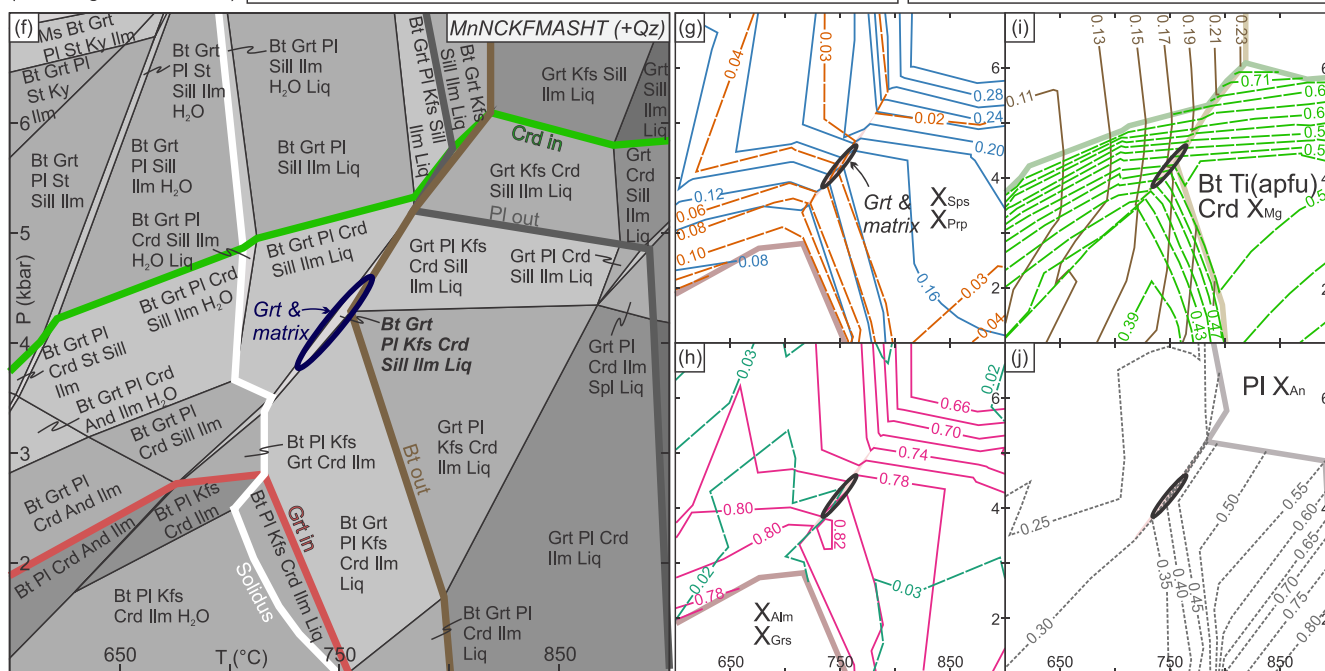


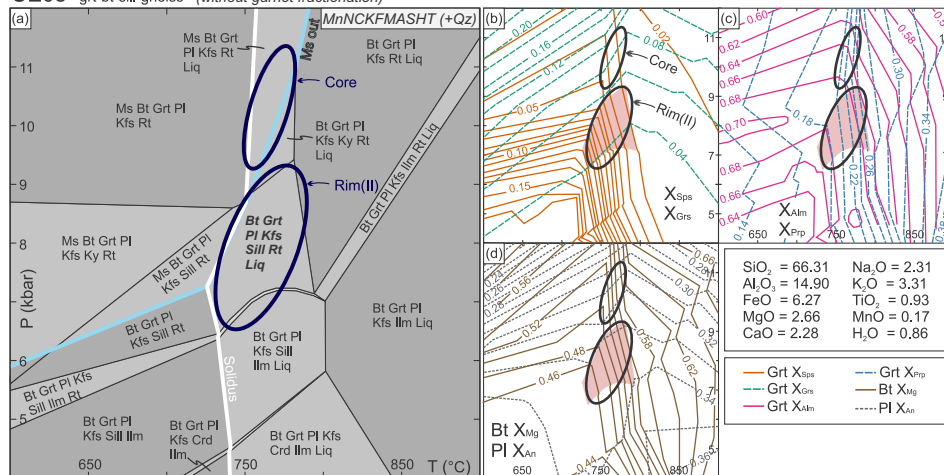
**FIGURE 6** (a) P–T Pseudosection for grt-sill-gneiss UB02 (whole-rock comp. in wt%). Estimated P–T conditions shown by black ellipses using the intersection of garnet and matrix mineral isopleths, and observed mineral assemblage in italics and bold. (b) Isopleths of Sps and Prp, (c) isopleths of Alm and Grs, (d) isopleths of Bt (Ti a.p.f.u) and (e) isopleths of Pl (X<sub>An</sub>). Matrix assemblage field shown in red. (f) P–T Pseudosection for grt-crd-gneiss UB22 (whole-rock comp. in wt%). (g) Isopleths of Sps and Prp, (h) isopleths of Alm and Grs, (i) isopleths of Bt (Ti a.p.f.u) and Crd (X<sub>Mg</sub>), and (j) isopleths of Pl (X<sub>An</sub>).

constrain P–T conditions, but the compositional isopleths for biotite (X<sub>Mg</sub> = 0.66–0.68) and plagioclase (X<sub>An</sub> = 0.15) intersect within a phase field containing the observed

mineral assemblage Bt–Pl–Kfs–Sil–melt and constrains matrix equilibration to 4.2–9.0 kbar and 670–770°C (circled in Figure 9a–c).



## UE08 grt-bt-sill-gneiss (without garnet fractionation)



## UE08 grt-bt-sill-gneiss (with garnet fractionation)

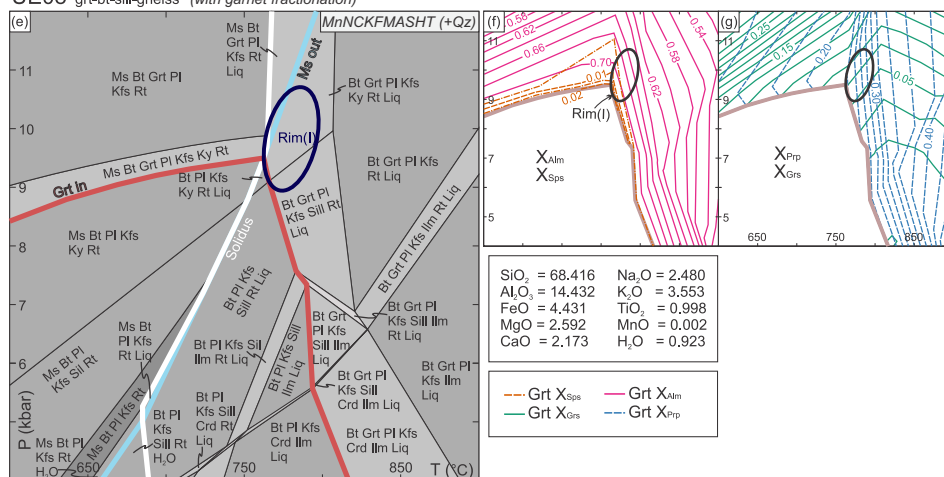


## FIGURE 7 (a) P-T

Pseudosection for grt-bt-sill-gneiss UE08 (whole-rock comp. in wt%). Estimated P-T conditions shown by black ellipses using the intersection of garnet core and rim II + matrix mineral isopleths. Observed mineral assemblage highlighted in *italics and bold*.

(b) Isopleths of Sps and Grs, (c) isopleths of Alm and Prp, (d) isopleths of Bt ( $X_{Mg}$ ) and Pl ( $X_{An}$ ). Matrix assemblage field shown in red. (e) P-T

Pseudosection for fractionated grt-bt-sill-gneiss UE08 (fractionated whole-rock comp. in wt%). Estimated P-T conditions shown by black ellipses using the intersection of garnet rim I isopleths. (f) Isopleths of Sps and Alm, (g) isopleths of Grs and Prp.

### 5.3 | Modelling samples from the Schist Belt

To estimate P-T conditions for samples UE14B and UD17, phase equilibrium models were calculated using measured bulk rock compositions to constrain conditions of early garnet growth. For both samples, garnet compositional isopleths for observed Sps, Alm, Prp, and Grs content in garnet cores (UE14B:  $Sps_{0.10}Alm_{0.75}Prp_{0.06}Grs_{0.08}$ ; UD17:  $Sps_{0.11}Alm_{0.73}Prp_{0.06}Grs_{0.1}$ ) constrain the temperature of early garnet growth to between  $\sim 525^{\circ}C$  and  $545^{\circ}C$  (Figure 10a,d). The intersecting isopleths do not provide a reliable pressure constraint, but the Grt-in line provides a minimum pressure constraint of  $\sim 4$  kbar. We infer that the garnet cores record earliest growth, and thus it is unlikely that the pressure conditions lie above  $\sim 6$  kbar where the Grt-in line deviates from the modelled compositional isopleths (Figure 10b,c,e,f).

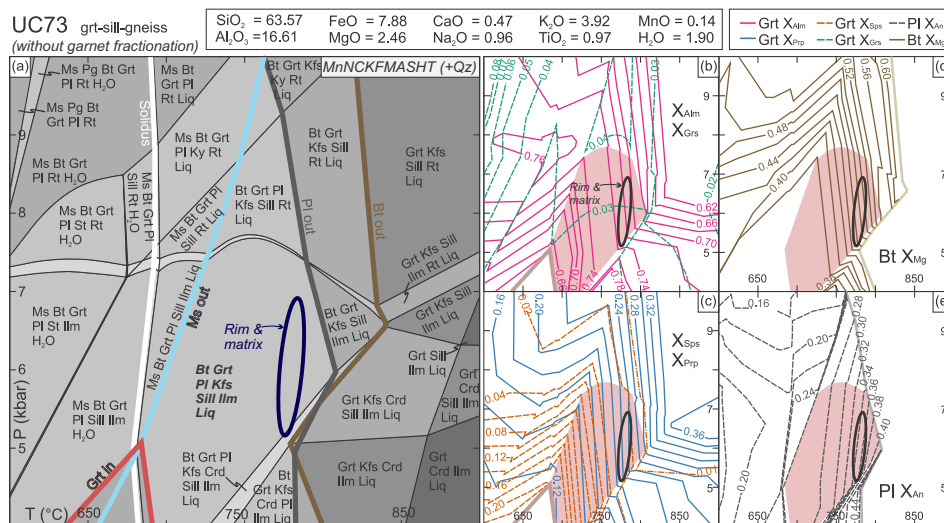
Exploratory garnet fractionation calculations using varying P-T values for the broad estimate for garnet core

conditions (data not shown) and the pseudosections calculated using the resulting fractionated bulk-rock compositions were shown to rapidly raise the pressure of the Grt-in line, but garnet fractionation did not significantly affect the position of calculated mineral isopleths for garnet rims and matrix minerals or the shapes of stability fields. This is likely due to low garnet mode ( $< 2$  vol.%), which should not significantly affect isopleth thermobarometry and necessitate garnet fractionation modelling (Lanari & Engi, 2017). The results of modelling with and without fractionation were thus seen to be nearly identical, and we conclude that the results using measured bulk compositions without garnet fractionation provide accurate estimates of matrix equilibration conditions.

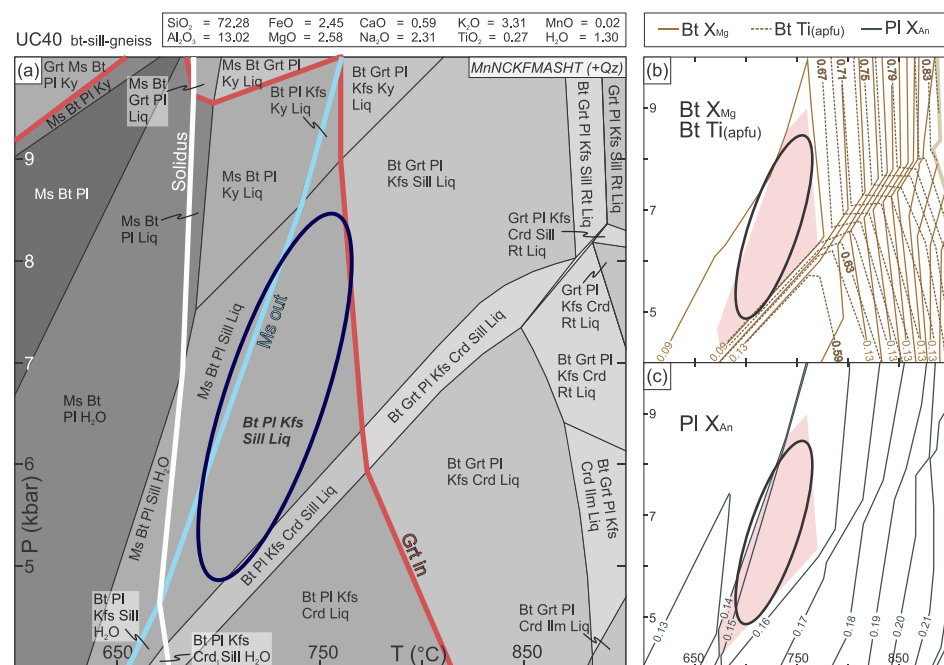
The pseudosection for sample UE14B is contoured for  $X_{Sps}$  and  $X_{Mg}$  in garnet (Figure 10b) and  $X_{Mg}$  in staurolite (Figure 10c). Compositional isopleths for garnet rims ( $Sps_{0.10}Alm_{0.75}Prp_{0.06}Grs_{0.10}$ ) and staurolite ( $X_{Mg} = 0.10-0.14$ ) intersect in a phase field containing the mineral assemblage Chl-Ms-Bt-Grt-St-Ilm, indicating peak P-T conditions of 6.0–7.0 kbar and 550–570°C (Figure 10a). The

**FIGURE 8** (a) P–T

Pseudosection for grt-sill-gneiss UC73 (whole-rock comp. in wt%). Estimated P–T conditions shown by black ellipses using the intersection of garnet rim and matrix mineral isopleths. Observed mineral assemblage highlighted in italics and bold. (b) Isopleths of Alm and Grs, (c) isopleths of Sps and Prp, (d) isopleths of Bt ( $X_{Mg}$ ), and (e) isopleths of Pl ( $X_{An}$ ). Matrix assemblage field shown in red.

**FIGURE 9** (a) P–T

Pseudosection for bt-sill-gneiss UC40 (whole-rock comp. in wt%). Estimated P–T conditions shown by black ellipses using the intersection of matrix mineral isopleths. Observed mineral assemblage highlighted in italics and bold. (b) Isopleths of Bt ( $Ti$  a.p.f.u. and  $X_{Mg}$ ), and (c) isopleths of Pl ( $X_{An}$ ). Matrix assemblage field shown in red.



observed mineral assemblage does not contain primary chlorite, suggesting that the true peak P–T conditions lie at slightly higher temperatures past the Chl-out line, or else the discrepancy can be attributed to error in the chlorite thermodynamic model.

The pseudosection for sample UD17 is contoured for  $X_{Sps}$ ,  $X_{Alm}$ ,  $X_{Prp}$ , and  $X_{Grs}$  in garnet and  $X_{Mg}$  in staurolite (Figure 10e,f). Compositional isopleths for garnet rims ( $Sps_{0.07}Alm_{0.80}Prp_{0.07}Grs_{0.06}$ ) and staurolite ( $X_{Mg} = 0.09–0.11$ ) intersect within a phase field containing the mineral assemblage Chl–Ms–Bt–Grt–St–Ilm, indicating peak P–T conditions of 5.5–6.5 kbar and 545–560°C (Figure 10d). Like sample UE14B, the observed mineral

assemblage does not contain primary chlorite, so the true peak P–T conditions likely reached slightly higher temperatures than is indicated in these models, at least past the Chl-out line.

## 6 | GEOCHRONOLOGY

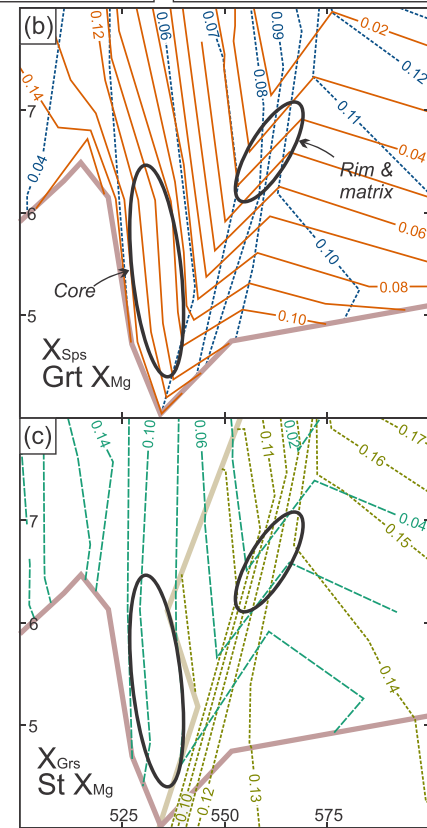
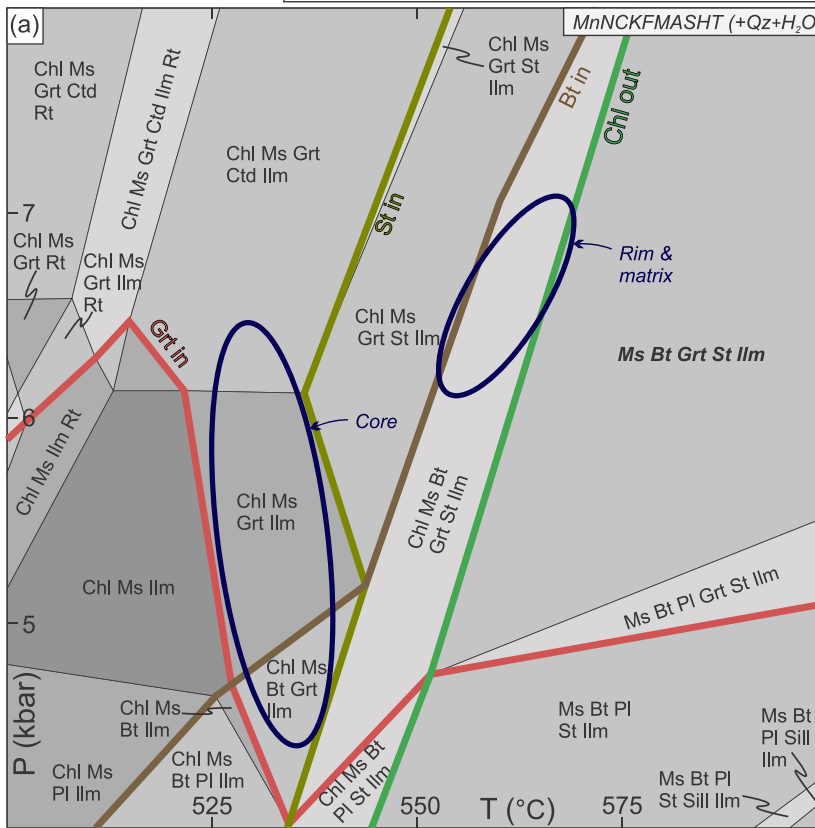
### 6.1 | Garnet Lu–Hf geochronology and trace element chemistry

Garnet–whole-rock Lu–Hf geochronology and trace element analysis was conducted at the Institute of

UE14B - grt-st-schist  
(without garnet fractionation)

SiO<sub>2</sub> = 65.63 FeO = 5.60 CaO = 0.50 K<sub>2</sub>O = 4.16 MnO = 0.04  
Al<sub>2</sub>O<sub>3</sub> = 18.01 MgO = 1.16 Na<sub>2</sub>O = 0.31 TiO<sub>2</sub> = 0.66

— Grt X<sub>Sps</sub> — Grt X<sub>Mg</sub>  
— Grt X<sub>Grs</sub> — St X<sub>Mg</sub>



UD17 - grt-st-schist  
(without garnet fractionation)

SiO<sub>2</sub> = 57.80 FeO = 7.52 CaO = 0.50 K<sub>2</sub>O = 4.54 MnO = 0.06  
Al<sub>2</sub>O<sub>3</sub> = 22.57 MgO = 1.46 Na<sub>2</sub>O = 0.26 TiO<sub>2</sub> = 0.90

— Grt X<sub>Sps</sub> — Grt X<sub>Alm</sub> — St X<sub>Mg</sub>  
— Grt X<sub>Grs</sub> — Grt X<sub>Prp</sub>

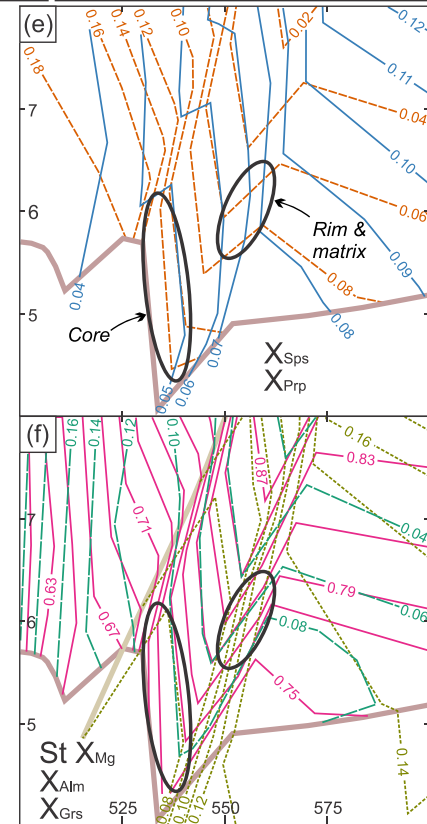
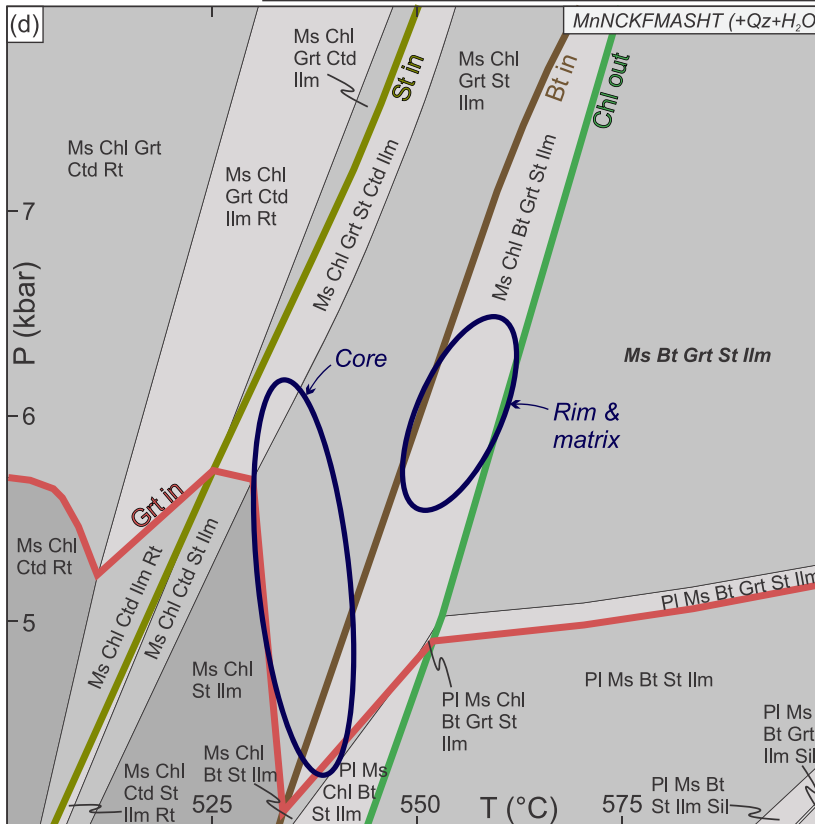


FIGURE 10 Legend on next page.



Geological Sciences, Polish Academy of Sciences, Kraków Research Centre. Sample preparation and isotopic analysis follow the methods from Anczkiewicz et al. (2004) and Anczkiewicz and Thirlwall (2003). Isotopic ratios were measured using ICP-MS Neptune by Thermo Scientific. The results are summarized in Table 1 and Figure 11a–c. Standards reproducibility and constants used for calculations are given in the footnote to Table 1. Lu–Hf isotope dilution analysis of three to four garnet fractions and one whole-rock fraction were used to define isochron ages for two gneisses from the Cerro Olivo Complex (samples UE08 and UB02) and one metapelitic schist from the Zanja del Tigre Complex (sample UE14B). The obtained isochron ages are  $654 \pm 23$  Ma (MSWD = 10.0) for sample UE08,  $638.5 \pm 2.2$  Ma (MSWD = 1.13) for sample UB02, and  $582 \pm 23$  Ma (MSWD = 8.3) for sample UE14B (Table 1 and Figure 11a–c).

Trace element concentrations were analysed along transects across representative garnet grains to determine the potential influence of mineral inclusions on isotope dilution results, and the influence of compositional zonation on the age interpretation. Analytical methods are detailed in Supporting Information Text S1. The results of trace element analysis from representative grains in samples UE08, UB02 and UE14B are summarized in Figure 11d–f.

Garnet from sample UB02 does not show consistent core–rim zonation between grains, although there is minor variation in relevant trace element concentrations across individual transects (Figure 11d). Despite an apparent lack of Hf-rich inclusions, Hf concentrations are particularly high, predominantly ranging between 1.0 and 3.0 ppm.

In contrast, garnet porphyroblasts from sample UE08 show consistent M-shaped Lu zonation, with a sharp increase in Lu close to the rim (Figure 11e). This zoning pattern matches that seen in the Mn concentration profile in Figure 5d. Regular dips in Lu concentration along the profile are due to Lu-poor mineral inclusions such as quartz, plagioclase and biotite (Figure 4i). Hf concentrations in inclusion-free parts of the garnet core and mantle are predominantly between 0.1 and 0.2 ppm, typical of metamorphic garnet (Anczkiewicz et al., 2014; Cheng, 2019; Scherer et al., 2000), whereas large peaks likely represent micro- to sub-micro-inclusions of Hf-rich phases such as zircon and titanite.

Garnet porphyroblasts from sample UE14B show strong bell-shaped Lu zonation, with peak concentrations of up to 500 ppm in the cores and decreasing dramatically towards the rims (Figure 11f). Hf concentrations are highly variable, but typically range between 0.2 and 0.5 ppm in clean parts of the garnet. Higher Hf concentrations along the profile are predominantly correlated with high-P alteration zones within cracks in the garnet, and to a lesser extent with narrow zones showing high concentrations of sub-micron inclusions of opaque oxides, likely ilmenite (Figure 11f).

## 6.2 | Interpretation of Lu–Hf garnet ages

Sample UB02 (fine-grained, Grt–Sil–gneiss from the Cerro Olivo Complex) shows good agreement between estimates of Hf concentration from isotope dilution versus LA–ICP–MS analysis (Figure 11, Table 1), indicating that the analytical results for this sample were not significantly affected by contamination from Hf-rich inclusions. Trace element profiles show relatively flat Lu trends (Figure 11d). Theoretical studies show that the closure temperature of Lu in garnet is lower for smaller grain sizes (Dodson, 1973; Ganguly & Tirone, 1999), such as those in sample UB02, which, combined with the high temperatures experienced by the sample, may be responsible for intracrystalline Lu diffusion (Anczkiewicz et al., 2012). Similarly, recrystallisation of garnet during peak temperature conditions may be responsible for the homogeneous trace element transect. Because of this, we interpret the Lu–Hf age obtained from sample UB02 ( $638.5 \pm 2.2$  Ma) as likely reflecting the timing of the high-T/low-P metamorphic event recorded in the matrix assemblage.

Samples UE08 (coarse-grained, Grt–Bt–Sil–gneiss from the Cerro Olivo Complex) and UE14B (Grt–St–schist from the Zanja del Tigre Complex), in contrast, show an order of magnitude difference in Hf concentration between isotope dilution analysis and LA–ICP–MS analysis of clean garnet. For sample UE08, the high Hf concentrations obtained by isotope dilution are likely due to contamination from Hf-rich inclusions in garnet such as titanite and zircon (Figure 11e). The acid dissolution method applied during sample preparation should ideally result in the removal of such inclusions from the analysed

**FIGURE 10** (a) P–T Pseudosection for grt–st–schist UE14B (whole-rock comp. in wt%). Estimated P–T conditions shown by black ellipses using the intersection of garnet and matrix mineral isopleths, and observed mineral assemblage in italics and bold. (b) Isopleths of Sps and Grt  $X_{Mg}$ , (c) isopleths of Grs and St ( $X_{Mg}$ ). (d) P–T Pseudosection for grt–st–schist UD17 (whole-rock comp. in wt%). (e) Isopleths of Sps and Prp, and (f) isopleths of Alm, Grs and St ( $X_{Mg}$ ).

TABLE 1 Summary of Lu–Hf dating results.

Sample	Sample weight (mg)	Lu (ppm)	Hf (ppm)	$^{176}\text{Lu}/^{177}\text{Hf}$	$^{176}\text{Hf}/^{177}\text{Hf}$	Age (Ma)
<b>UE08</b>						
Grt1	80.27	4.587	3.562	0.1822	$0.284262 \pm 4$	$654 \pm 23$
Grt2	81.49	4.147	2.846	0.2061	$0.284590 \pm 4$	
Grt3	82.52	4.020	3.118	0.1824	$0.284313 \pm 3$	
Grt4	83.01	4.016	3.048	0.1864	$0.284351 \pm 4$	
WR	101.33	0.449	2.853	0.0223	$0.282327 \pm 3$	
<b>UB02</b>						
Grt1	68.90	6.736	2.052	0.4647	$0.287730 \pm 6$	$638.5 \pm 2.2$
Grt2	66.02	7.059	2.157	0.4633	$0.287730 \pm 4$	
Grt3	79.39	8.674	2.744	0.4475	$0.287554 \pm 4$	
WR	99.61	0.474	1.430	0.0468	$0.282735 \pm 3$	
<b>UE14B</b>						
Grt1	62.15	26.094	2.131	1.7349	$0.301051 \pm 5$	$582 \pm 23$
Grt2	62.14	25.681	2.068	1.7624	$0.301201 \pm 3$	$(584.0 \pm 2.4)^a$
Grt3	67.56	23.333	1.962	1.6890	$0.300227 \pm 5$	
WR	100.48	0.336	3.881	0.0123	$0.282065 \pm 4$	

Note: All errors are 2 SE (standard errors) and relate to the last significant digits.  $^{176}\text{Lu}/^{177}\text{Hf}$  errors are 0.5%. JMC475 yielded  $^{176}\text{Hf}/^{177}\text{Hf} = 0.282164 \pm 4$  ( $n = 8$ ) over the period of analysis. Mass bias corrections conducted using  $^{179}\text{Hf}/^{177}\text{Hf} = 0.7325$ . Decay constants used for age calculations:

$\lambda^{176}\text{Lu} = 1.865 \times 10^{-11} \text{ year}^{-1}$  (Scherer et al., 2001). Age uncertainties are  $2\sigma$ .

<sup>a</sup>Age calculated with three point isochron excluding Grt3.

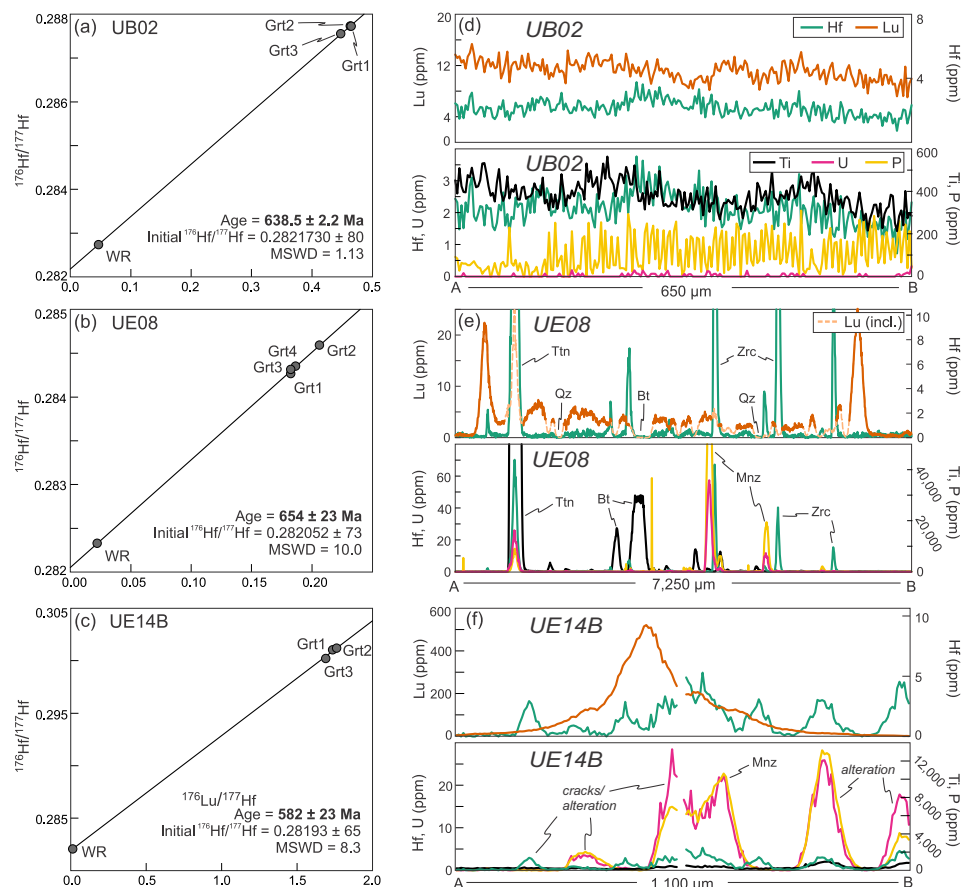
sample, yet metamict zircon present in the garnet could be dissolved during this process and thus influence the Hf budget. The zircon from this sample look to be in good condition (e.g., Figure 12e–h), and the majority of grains analysed for U–Pb dating overlap within error with the garnet Lu–Hf age (see section 6.3) suggesting that zircon is likely in isotopic equilibrium with garnet. However, zircon is present in sufficient volume that it is difficult to rule out contamination from sub-micron inclusions containing inherited Hf. In any case, it is likely that inclusions in garnet are responsible for the low  $^{176}\text{Lu}/^{177}\text{Hf}$  ratios from sample UE08, which is in turn responsible for the low precision of the isochron age (Table 1).

However, considering the differing P–T conditions between garnet core growth and rim equilibration (see Figure 9a–c), it is possible that the high imprecision is the result of age disparity between the different garnet zone domains, and thus the age of  $654 \pm 23$  Ma may represent an average age of prolonged growth and/or the effects of diffusive relaxation of garnet rims at high temperatures. Additionally, the enrichment of Lu near garnet rims is suggestive of garnet resorption resulting in the preferential uptake and fractionation of Lu relative to Hf. This would have the effect of producing a younger apparent age skewed towards the timing of the resorption

event (Kelly et al., 2011), although this bias is likely insignificant relative to the age uncertainty. Despite these complications, the ages obtained from samples UB02 and UE08 overlap within error.

Sample UE14B similarly shows higher Hf concentration from isotope dilution analysis compared with LA–ICP–MS analysis of clean garnet. Contamination from alteration products in micro-cracks is unlikely, considering the effort to remove impure fragments by manual picking, ultrasonic bath treatment, and through acid leaching. It is more likely that Hf contamination comes from high-density sub-micron inclusions of ilmenite, which have a higher chance of evading removal but which should not pose a problem in the accuracy of the isochron age. Furthermore, due to high Lu concentrations in the garnet (Table 1 and Figure 11f), we obtained high  $^{176}\text{Lu}/^{177}\text{Hf}$  ratios, meaning that it is unlikely that Hf contamination had a significant effect on age precision. Despite this, the resulting four-point isochron shows a large error and large MSWD, which appears to be due to a single garnet fraction (Grt3). Removing this anomalous fraction results in a higher precision age of  $584.0 \pm 2.4$  Ma (Table 1), although analytically there is no known problem with this fraction and so the low precision age will be considered throughout the rest of the text. Considering the prograde, bell-shaped distribution

**FIGURE 11** Garnet-whole-rock Lu–Hf isochrons for samples (a) UB02, (b) UE08 and (c) UE14B, and LA-ICP-MS line scans (Lu, Hf, U, Ti and P) along representative garnet grains from samples (d) UB02, (e) UE08, and (f) UE14B. The dashed, light orange line in (e) denotes the Lu concentration measured from inclusions within garnet, highlighting the M-shaped zonation profile found within the pure garnet of sample UE08. Images of garnet transects for (d), (e), and (f) are shown in Figure 4i,e,a, respectively.



of Lu in garnet, we interpret the isochron age of  $582 \pm 23$  Ma as being biased towards the timing of early garnet growth in sample UE14B.

### 6.3 | U–Pb zircon and monazite geochronology

Zircon and monazite grains were analysed for U–Pb age dating to complement garnet Lu–Hf ages in the Cerro Olivo Complex, as well as to determine the timing of metamorphism in the Campanero Unit. Before analysis, cathodoluminescence (CL) and back scattered electron (BSE) images of zircon and monazite grains, respectively, were taken to allow the targeting of specific areas and structures. Zircon U–Pb data were analysed at the Institute of Geology of the Czech Academy of Sciences, Prague, Czech Republic, using laser ablation inductively coupled plasma mass spectrometry (LA–ICP–MS). Monazite U–Pb data and zircon U–Pb data from one sample (UA38) were analysed at the NordSIMS facility at the Swedish Museum of Natural History in Stockholm using secondary ion mass spectrometry (SIMS). Analytical methods and further details are presented in Text S1 and

Table S5. Analytical data tables are also available in the supporting information.

#### 6.3.1 | Zircon U–Pb ages from the Cerro Olivo Complex

Zircon grains from sample UB02 are  $\sim 150$ – $250$   $\mu\text{m}$  in length and are predominantly rounded and anhedral in shape (Figure 12). Most grains show weak, patchy zoning (Figure 12a,b), or show no zoning at all (Figure 12c), although grains with oscillatory zoning are not uncommon. Grains with oscillatory zoning almost always have overgrowth rims of varying thickness (Figure 12d). From LA–ICP–MS isotopic analysis of 56 spots on zircon, 6 provided  $>10\%$  discordant dates and were not considered further. From the remaining 50 dates (Figure 13a), 40 closely clustered dates combine to give a concordia age of  $649.0 \pm 5.6$  Ma (Figure 13b). The remaining dates are individually scattered up to c. 800 Ma, with a minority of individual dates younger than c. 640 Ma that are considered as outliers and not significant. The c. 650 Ma dates come from the weakly- to un-zoned grains and overgrowth rims, whereas the older dates come from



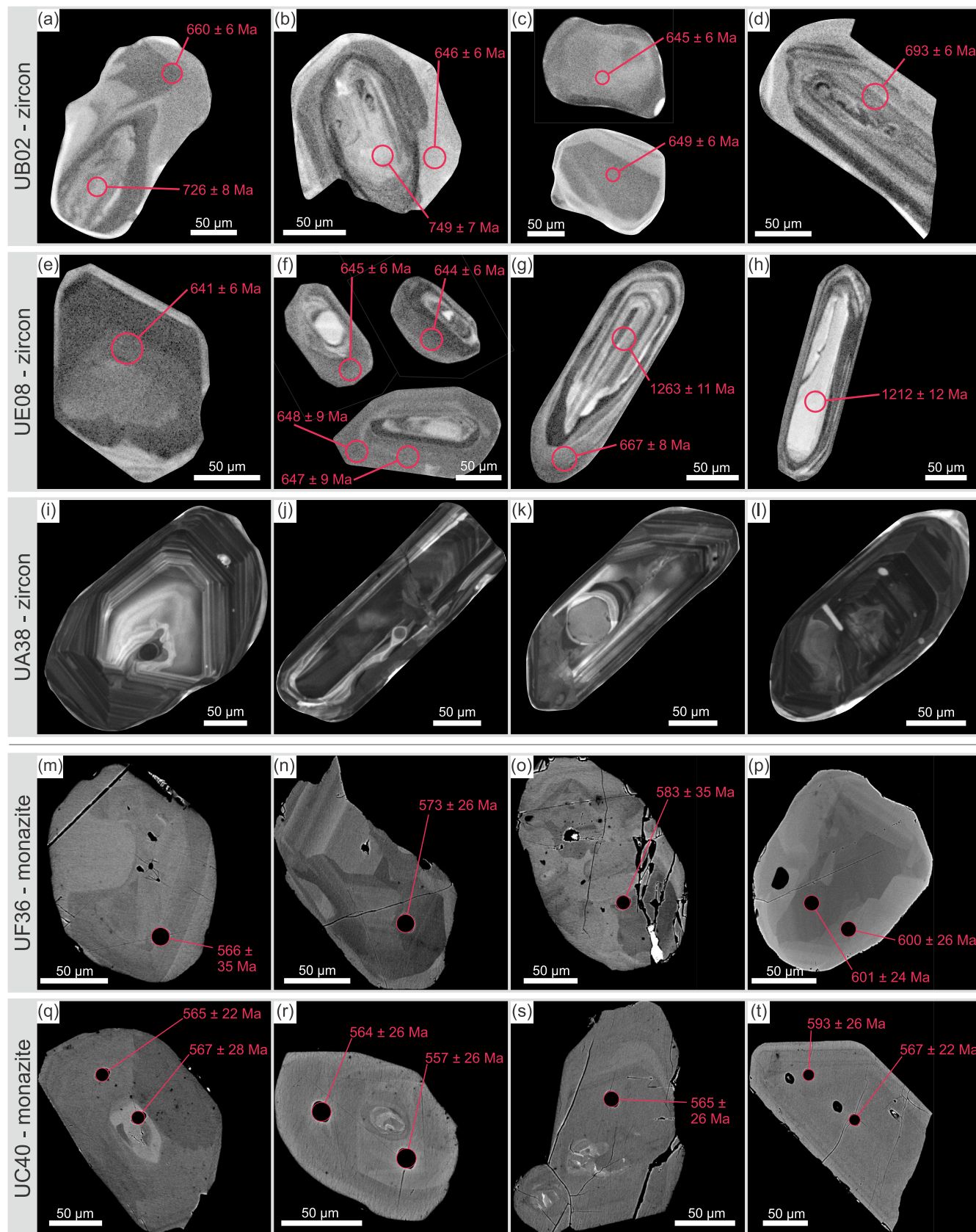


FIGURE 12 Legend on next page.

grains and cores with well-defined, oscillatory zoning (Figure 12a–d). Based on these observations, we interpret the c. 650 Ma concordia age as reflecting the timing of granulite facies metamorphism, whereas the remaining older dates are likely inherited grains from a previous event at c. 800 Ma.

Zircon grains from sample UE08 are between ~100 and 250  $\mu\text{m}$  in length, and are predominantly long, euhedral crystals, although a subordinate number of grains are short and oval-shaped, occasionally with rounded edges (Figure 12e–h). A few grains show no internal zoning, or very small, zoned cores (Figure 12e,f), whereas most of the grains show oscillatory zoning with thin, featureless overgrowth rims (Figure 12g,h). From LA-ICP-MS isotopic analysis of 70 spots, 10 provided >10% discordant dates and thus were not considered further. From the remaining 60 dates (Figure 13c), two clusters of dates are observed at c. 650 and c. 1,250 Ma. The younger discordant cluster produced a discordia line with a lower intercept of  $641.6 \pm 2.8$  Ma (Figure 13d). A small cluster (six analyses) of <1% discordant dates produced a concordia age of  $645.9 \pm 6.2$  Ma (Figure 13e), overlapping within error with the intercept age. The younger cluster of dates (<700 Ma) come from zircon grains with only weak zoning, or from overgrowth rims around strongly zoned cores (Figure 12e–h). The older dates are from zircon grains showing oscillatory zoning, both with and without overgrowth rims. Based on these observations, we interpret the concordia and discordia ages as reflecting the timing of metamorphism, whereas the remaining older dates are likely inherited detrital grains.

Zircon grains extracted from the deformed porphyritic granite sample UA38 are c. 100–170  $\mu\text{m}$  long (Figure 12i–l). CL images revealed that the grains are mostly oscillatory-zoned and have no significant inherited cores. Some grains have CL-bright and mostly <10- $\mu\text{m}$ -thick rims that may represent metamorphic overgrowths (Figure 12i,l). LA-ICP-MS isotopic analysis of the zircon (25 analytical spots taken from oscillatory-zoned regions) yielded a concordia U–Pb age of  $656 \pm 4$  Ma (Figure 13f), and nine SIMS analyses in oscillatory-zoned parts of the grains combine in a concordia U–Pb age of  $654 \pm 3$  Ma (Figure 13g). Both ages are indistinguishable within error. Considering the degree of deformation and recrystallisation seen in the sample (Figure 3c) it is unlikely that the metamorphic event

completely overprinted older igneous zircon, thus we interpret this as the igneous protolith age of the sample.

### 6.3.2 | Monazite and zircon U–(Th)–Pb ages from the Campanero Unit

Monazite grains from Bt-gneiss sample UF36 are predominantly rounded and reach ~100–200  $\mu\text{m}$  in length. Irregular, cloudy internal zoning (Figure 12m–p) suggests growth during metamorphism (Schulz, 2021). SIMS analysis of 21 analytical spots from 16 grains provide data that combine to give a U–Pb concordia age of  $582.7 \pm 5.7$  Ma (Figure 13h). The  $^{208}\text{Pb}/^{232}\text{Th}$  weighted mean age from the same analyses provides an age of  $572.1 \pm 7.8$  Ma (Figure 13j), overlapping within error with the U–Pb concordia age. We interpret this age as reflecting the timing of peak metamorphism, although without further geochemical constraints it is difficult to rule out growth during the exhumation/cooling phase.

Monazite grains from the melanocratic–mesocratic part of Bt-Sil-gneiss sample UC40 are c. 100–190  $\mu\text{m}$  in length, and often show concentric or sector zoning with rounded to euhedral crystal shapes (Figure 12q–t). Despite the chemical zonation observed in BSE images, there is no distinct age zonation in any of the grains. SIMS analysis of 19 analytical spots from 10 grains provided data that combine in a concordia U–Pb age of  $572.1 \pm 5.2$  Ma (Figure 13i). The  $^{208}\text{Pb}/^{232}\text{Th}$  weighted mean age from the same analyses provides an age of  $574.9 \pm 7.6$  Ma (Figure 13k), similarly overlapping with the U–Pb concordia age. Based on the matrix equilibration conditions estimated from PT modelling, the absence of evidence for significant retrograde re-equilibration, and the presence of a single age population, we interpret this age as reflecting the timing of peak metamorphism.

Zircon grains separated from the leucocratic portion of sample UC40 rock are c. 130–300  $\mu\text{m}$  long. CL imaging reveals that all grains are either entirely oscillatory-zoned, or they show oscillatory-zoned outer parts surrounding indistinct sector-zoned or featureless cores. From 46 grains analysed by LA-ICP-MS, 20 of them provided >10% discordant dates and these were not considered further. The remaining 26 analytical spots yielded a spectrum of dates, with one cluster around c. 630 Ma and the rest spread across the Mesoproterozoic–Archean

**FIGURE 12** (a–l) Cathodoluminescence images of analysed zircon from samples UB02 (a–d), UE08 (e–f), and UA38 (i–l) from the Cerro Olivo complex, with analysed spots and  $^{206}\text{Pb}/^{238}\text{U}$  ages ( $2\sigma$  error) indicated for samples UB02 and UE08. (m–t) Back-scattered electron (BSE) images of monazite from samples UF36 (m–p) and UC40 (q–t) from the Campanero Unit, with analysed spots and  $^{206}\text{Pb}/^{238}\text{U}$  ages ( $2\sigma$  error) indicated.



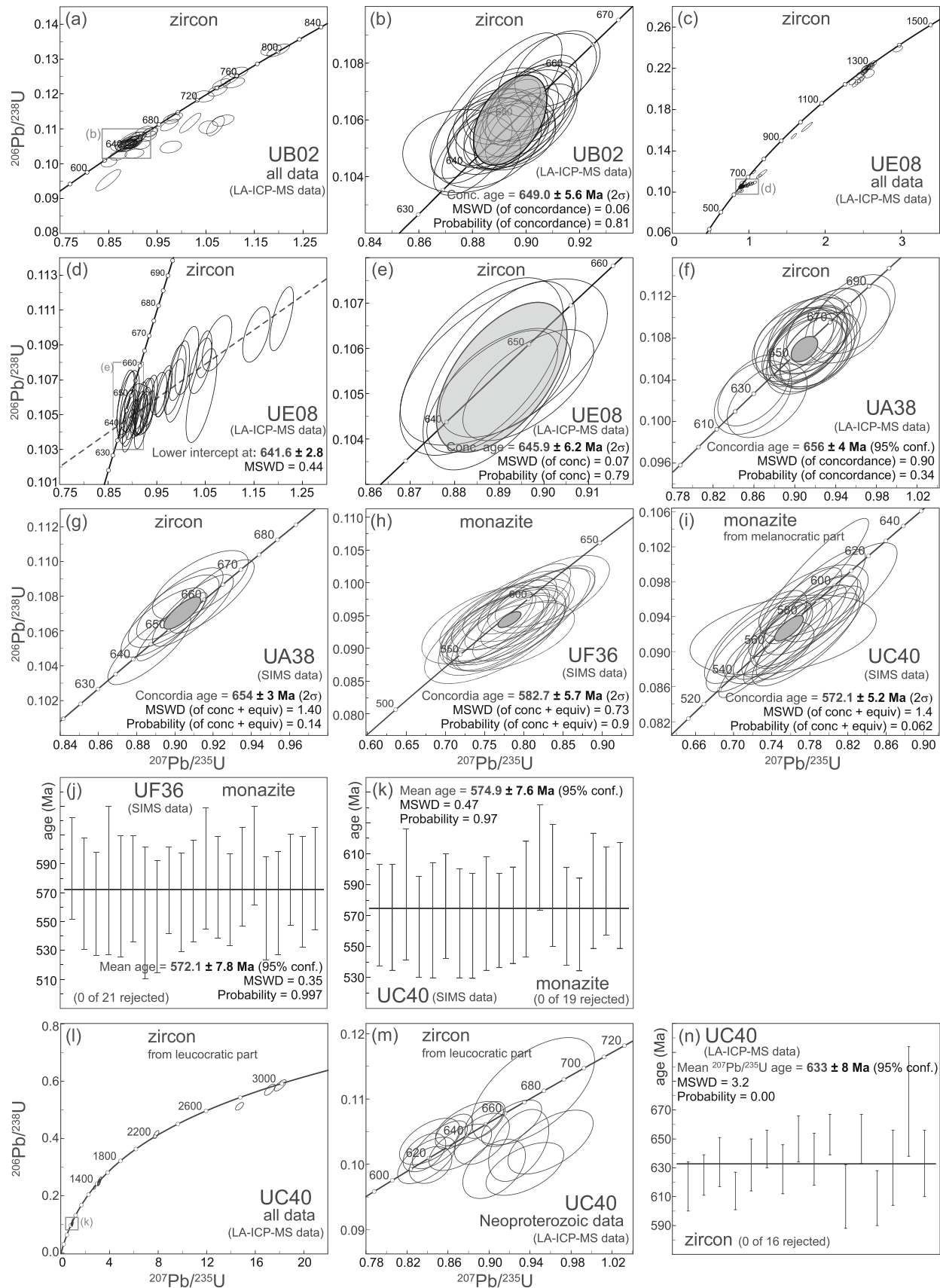


FIGURE 13 Legend on next page.

(Figure 13l). The scatter of the Neoproterozoic cluster did not allow calculation of a concordia age (Figure 13m). However, the  $^{206}\text{Pb}/^{238}\text{U}$  dates of the youngest cluster combine into a weighted average mean age of  $633 \pm 8$  Ma (95% conf.), which we interpret as being rather imprecise and probably inaccurate, but still the best estimate of the crystallization of the leucocratic part of the rock (Figure 13n). The remaining dates between c. 1.36 and 3.00 Ga are interpreted as coming from inherited, xenocrystic grains.

## 7 | DISCUSSION

### 7.1 | P–T–t paths and the tectonic evolution of the southern Dom Feliciano Belt

#### 7.1.1 | The hinterland—Cerro Olivo Complex

The P–T–t data collected in this study are summarized in Figure 14. Thermodynamic modelling of metamorphic conditions for gneisses of the Cerro Olivo Complex suggests their near-isothermal decompression at  $\sim 750$ – $800^\circ\text{C}$  from upwards of  $\sim 10$ – $11$  kbar down to  $\sim 5.5$ – $8$  kbar (D1). The  $\sim 10$ – $11$  kbar pressure estimate from sample UE08 is the only preserved record of earlier, higher pressure conditions in these rocks, and suggests burial to a minimum depth of  $\sim 35$ – $40$  km. Otherwise, all but one of the analysed samples record matrix equilibration at the lower pressure conditions of  $\sim 5.5$ – $8$  kbar, implying that this metamorphic event is ubiquitous across the complex and is likely associated with the observed dominant S1 high-temperature deformation fabric. Evidence of further decompression is recorded in one sample (grt-crd-gneiss UB22), which shows matrix equilibration conditions of  $\sim 750$ – $780^\circ\text{C}$  and  $\sim 4.0$ – $4.5$  kbar. This sample shows no record of previous metamorphic equilibration conditions, and so decompression from higher pressures ( $\sim 5.5$ – $8$  kbar) is inferred from the

similarity in temperature estimates of the other granulite facies samples, and the absence of any geochronological evidence supporting a later high-T metamorphic event. Our data generally support previous P–T estimates of Gross et al. (2009), who found the same three-stage clockwise metamorphic path using combined conventional thermobarometry and phase equilibria modelling, although with somewhat differing results. Notably, their data suggest higher temperatures for the peak pressure phase ( $830$ – $950^\circ\text{C}$ ), and lower temperatures for the late decompression phase ( $600$ – $750^\circ\text{C}$ ), but despite this their P–T estimates mostly overlap with those from this study. The data also fit with peak pressure estimates of  $>10$  kbar from Will et al. (2020).

The two garnet Lu–Hf isochron ages (UB02:  $638.5 \pm 2.2$  Ma; UE08;  $654 \pm 23$  Ma), despite high imprecision from one of the samples, provide strong evidence to constrain high-T metamorphism of the Cerro Olivo Complex between c. 655 and 640 Ma. Although the prograde metamorphic history related to crustal thickening is not preserved in any of the studied Cerro Olivo samples, the elevated pressure conditions preserved in the compositional profile of garnet in the Grt-Bt-Sil-gneiss sample UE08, which probably represents garnet growth zoning strongly modified by diffusion (Caddick et al., 2010), suggests that the older age of  $654 \pm 23$  Ma may correspond to the timing of earliest crustal thickening in the hinterland domain. As pre-orogenic rifting is estimated to have ended only by c. 660–650 Ma (Hoffman, 2021; Konopásek et al., 2020), convergence and crustal thickening likely shortly followed crustal thinning. Thus, the burial of the hinterland domain to depths of at least c. 40 km (Figure 14a) and the intrusion of porphyritic granites (e.g., sample UA38) suggests significant thickening of an already hot, thinned crust at c. 655 Ma, coeval with the timing of crustal thickening recorded in the northern Dom Feliciano Belt (Percival et al., 2022). The garnet from sample UB02, on the other hand, does not show evidence for the preservation of an earlier higher-pressure metamorphic event, and thus the garnet Lu–Hf age of  $638.5 \pm 2.2$  Ma from this sample is the best estimate

**FIGURE 13** Results of U–Pb dating in zircon and monazite for samples from the Cerro Olivo complex (a–g) and the Campanero Unit (h–l). Wetherill concordia and weighted mean diagrams are as follows: (a) overview of all zircon data ( $<10\%$  discordant) in sample UB02; (b) concordia age for sample UB02; (c) overview of all zircon data ( $<10\%$  discordant) in sample UE08; (d) discordia age for sample UE08 (with calculated excess variance); (e) concordia age for sample UE08 (with calculated excess variance); (f) concordia age for zircon in sample UA38 (SIMS data); (g) concordia age for zircon in sample UA38 (LA-ICP-MS data); (h) concordia age for monazite in sample UF36; (i) concordia age for monazite in melanocratic sample UC40; (j) weighted mean  $^{208}\text{Pb}/^{232}\text{Th}$  age from monazite in sample UF36 (wtd by data-pt errors only); (k) weighted mean  $^{208}\text{Pb}/^{232}\text{Th}$  age from monazite in sample UC40 (wtd by data-pt errors only); (l) overview of all zircon ( $<10\%$  discordant) in leucocratic sample UC40; (m) young cluster of zircon data in leucocratic sample UC40; (n) weighted mean  $^{206}\text{Pb}/^{235}\text{U}$  age from zircon in leucocratic sample UC40. Error ellipses and error bars are plotted at  $2\sigma$  level. MSWD is the mean square of weighted deviates.



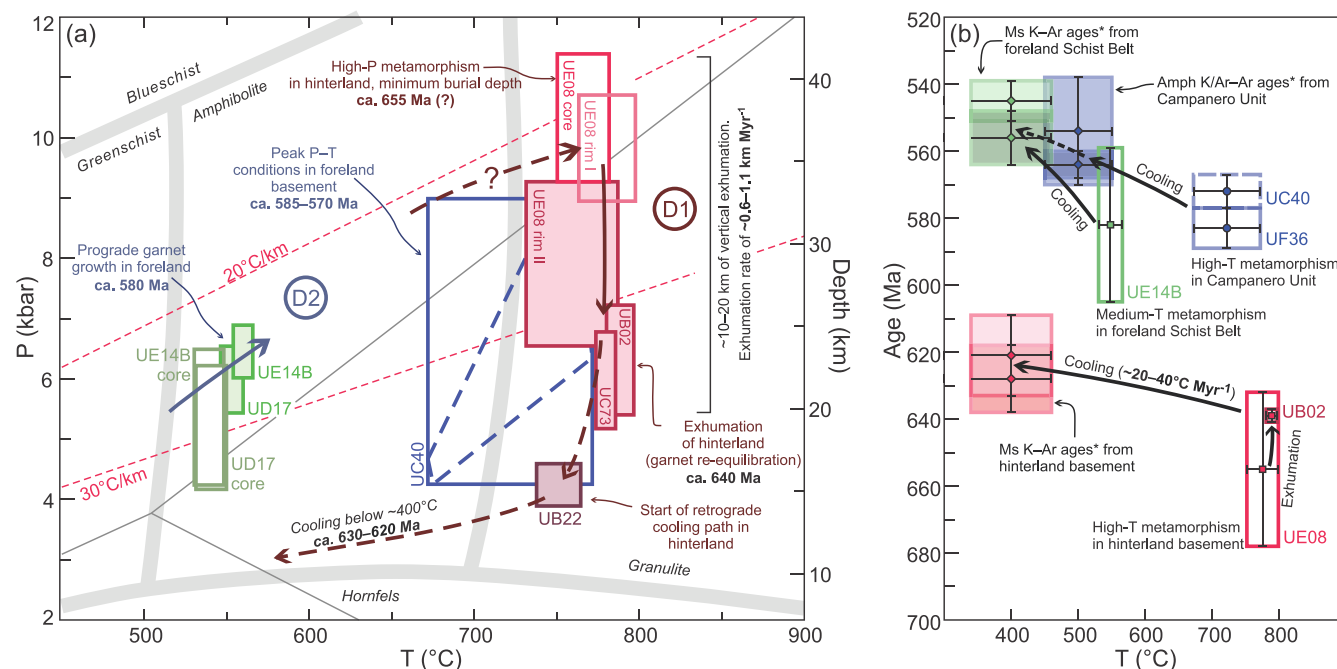


**FIGURE 14** (a) Summary of P-T-t paths based on pseudosections and geochronological data from this study. D1—garnet cores record peak pressures in the hinterland, followed by near complete re-equilibration of rocks during exhumation. Cooling in the hinterland by c. 630 Ma based on Oyhantçabal et al. (2009) and Will et al. (2019). D2—prograde garnet growth recorded in foreland supracrustal rocks, following a geothermal gradient of  $\sim 25^{\circ}\text{C}/\text{km}$ . Evidence of D1 not observed in the foreland. (b) Cooling paths for the hinterland and foreland (\* denotes K-Ar ages from Oyhantçabal et al. (2009); closure temperature ranges from Harrison et al. (2009); McDougall and Harrison (1999)). Note the rapid cooling of the hinterland following exhumation, and intersection of the cooling path of the foreland basement with the foreland Schist Belt.

for the timing of metamorphism responsible for the development of S1 and L1; namely high-T/low-P metamorphism during decompression and E-W directed tectonic transport. The growth of zircon in sample UE08, which are dated within error of the garnet from UB02 (U-Pb zircon intercept age of  $641.6 \pm 2.8$  Ma and concordia age of  $645.9 \pm 6.2$  Ma), likely records this same metamorphic event. The U-Pb zircon age of  $649.0 \pm 5.6$  Ma derived from sample UB02 is a noticeable discrepancy, as it is c. 10 Ma older than the Lu-Hf garnet age from the same sample, and shows a closer fit to the protolith age obtained from the orthogneiss sample UA38 ( $654 \pm 3$  SIMS and  $656 \pm 4$  Ma LA-ICP-MS). It is possible that the zircon age records earlier prograde metamorphism prior to the lower-P re-equilibration evident in the garnet and matrix. However, considering that most zircon grains in sample UB02 contain c. 800 Ma cores, the shift towards a slightly higher U-Pb concordia age (Figure 13a) can also be explained by incomplete lead loss from protolith zircon. The same situation is seen in the discordant dates from sample UE08, but as the protolith zircon grains in this sample are much older it is easier to see that the younger, re-equilibrated metamorphic dates are discordant and plot away from the true age (Figure 13d).

The data as presented point towards high temperature metamorphism and partial melting between c. 655 and 640 Ma. The intrusion of porphyritic granites (such as sample UA38, and at localities UB26 and UA42) at c. 655 Ma, and coeval medium-P/high-T granulite facies metamorphism, marks the earliest phase of crustal thickening during orogenesis (Figure 15a). We interpret the subsequent isothermal decompression as following a clockwise P-T path, reflecting the exhumation of the orogenic hinterland during progressive thrusting over the foreland. Calculating the difference between the peak and re-equilibration pressures (using UE08 garnet core and UB02 matrix P-T estimates) gives a decompression path of 2.5–6.2 kbar, which translates to a vertical exhumation of  $\sim 10$ –20 km (using an average crustal density of  $2.8 \text{ g}/\text{cm}^3$ ). Dividing these values by the duration of exhumation ( $17.5 \pm 4.5$  Ma; calculated using the estimated metamorphic peak at  $656.0 \pm 4.0$  Ma (UA38) and low-P overprint at  $638.5 \pm 2.2$  Ma (UB02)) results in an exhumation rate of between 0.6 ( $+0.2/-0.1$ ) and 1.1 ( $+0.4/-0.2$ )  $\text{km Ma}^{-1}$  (Figure 14a). These rates are relatively slow (e.g., Štípská et al., 2004; Tajčmanová et al., 2006), supporting the fact that almost no relict higher-P mineral assemblages are preserved.

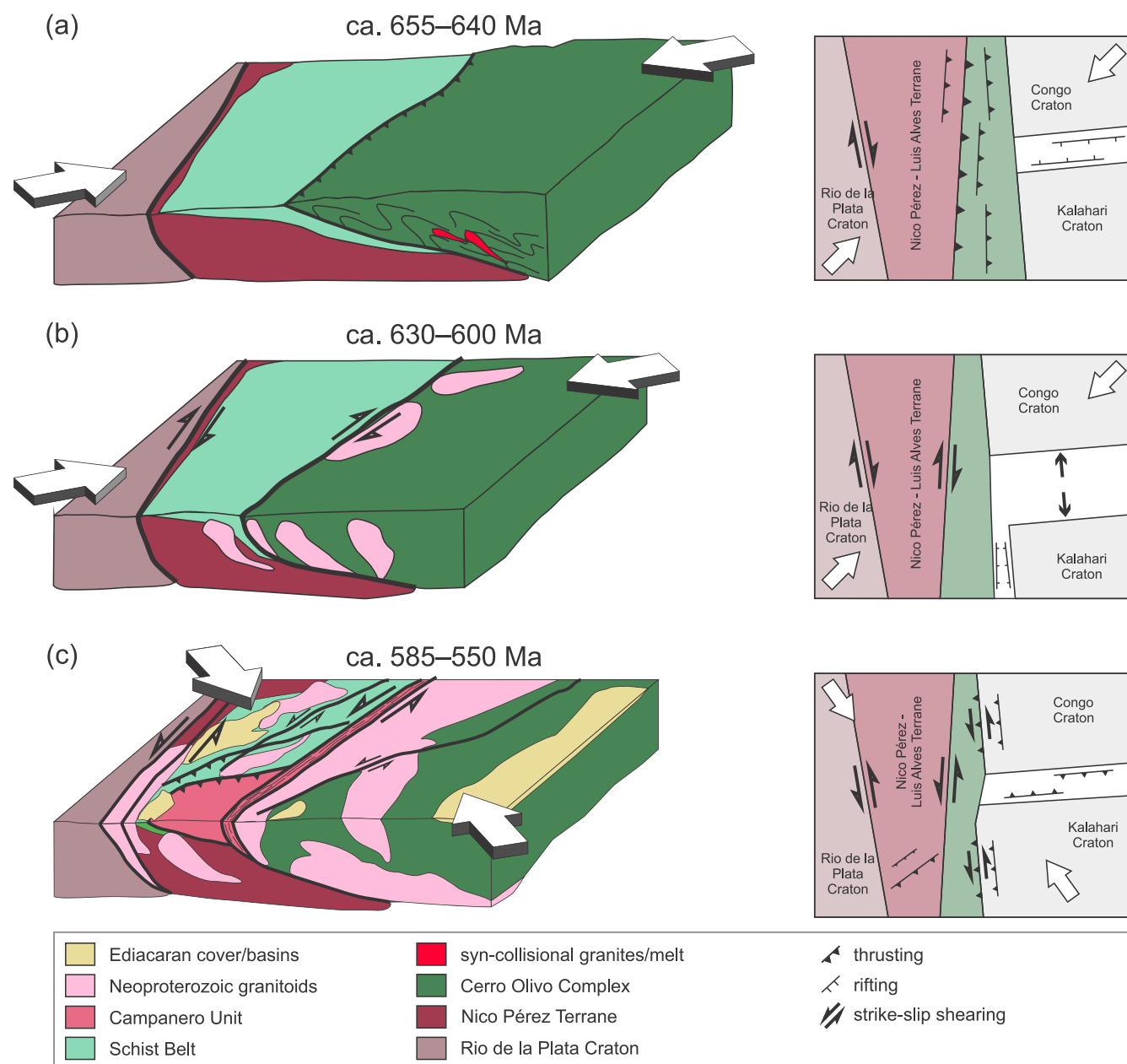


**FIGURE 15** Schematic interpretation of the Neoproterozoic evolution of the southern Dom Feliciano Belt (block diagrams on left) and the wider Kaoko–Dom Feliciano–Gariep orogenic system (map view diagrams on right). (a) Oblique convergence between the Nico Pérez terrane and the Congo craton from at least c. 655 Ma results in burial, high-T metamorphism (including partial melting), then exhumation of the Cerro Olivo complex. (b) Continuing convergence between c. 630 and 600 Ma results in transition to a transpressional system with the development of large-scale dextral strike-slip shear zones along major tectonic boundaries (possibly coincides with rifting of the Kalahari craton; Hoffman, 2021). (c) Switch to predominantly sinistral transpression from c. 585 Ma driven by oblique convergence of the Kalahari craton, resulting in renewed orogenic activity in the Dom Feliciano Belt (thrusting, metamorphism, and granite intrusion in the southern foreland), as well as large-scale transpressional orogenesis in the Kaoko Belt.

Our geochronological data closely match metamorphic age constraints from Lenz et al. (2011) and Oyhançabal et al. (2009), who presented zircon U–Pb concordia ages from metamorphic rims in Cerro Olivo Complex gneisses of  $653 \pm 4$  and  $641 \pm 17$ , respectively. Will et al. (2019) presented similar U–Pb zircon rim concordia ages of

between c. 655 and 642 Ma, as well as closely matching U–Pb monazite intercept ages of  $647 \pm 11$ ,  $639 \pm 9$ , and  $632 \pm 12$ . We interpret the few individual zircon grains in sample UB02 that record ages between c. 660 and 670 Ma as not statistically significant, and thus we do not consider them to be an adequate estimate of earliest



metamorphism and crustal thickening, such as is suggested by Lenz et al. (2011) and Masquelin et al. (2011) based on similar age distributions in their samples. Furthermore, and as previously mentioned, the shift towards higher ages in some of these samples likely represents incomplete lead loss from Tonian-aged cores, and thus does not record true metamorphic ages.

Following exhumation, cooling of the hinterland below  $\sim 400^{\circ}\text{C}$  was reached by c. 630–620 Ma (Figures 14 and 15b), as constrained by K–Ar cooling ages in muscovite and Ar–Ar cooling ages in hornblende (Oyhantçabal et al., 2009; Will et al., 2019). The cooling rate is difficult to estimate due to overlapping age estimates, but by using the Lu–Hf garnet age and temperature estimate from sample UB02 ( $638.5 \pm 2.2$  Ma,  $\sim 790^{\circ}\text{C}$ ), and ignoring the errors associated with the two muscovite K–Ar cooling ages from Oyhantçabal et al. (2009) ( $628 \pm 10$  and  $621 \pm 12$  Ma), we obtain a roughly-estimated cooling rate of between 20 and  $45^{\circ}\text{C Ma}^{-1}$  (Figure 14b).

### 7.1.2 | The foreland – Campanero Unit and Schist Belt

Thermodynamic modelling of the migmatitic Campanero Unit indicates metamorphic equilibration conditions between  $\sim 670$ – $770^{\circ}\text{C}$  and  $\sim 4$ – $9$  kbar, showing that the unit reached high enough temperatures for partial melting. Although the results overlap with those from the dominant P–T conditions recorded in the Cerro Olivo Complex (Figure 14a), the estimate is largely imprecise. In contrast with the Cerro Olivo Complex, the rocks in the Campanero Unit have the appearance of uppermost amphibolite-facies gneisses, and thus it is likely the true temperature conditions are on the lower end of this estimate. The imprecise weighted mean zircon U–Pb age of  $633 \pm 8$  from the leucocratic parts of sample UC40 suggests an early partial melting event recorded in the Campanero Unit that may be temporally related to the high-T metamorphism in the hinterland formed during early crustal thickening (D1). This could explain the NW–SE orientation of stretching lineation L1 preserved in the Campanero gneisses (Figure 2c), which likely formed during a similar, roughly E–W-directed tectonic transport as within the Cerro Olivo Complex. However, this age more closely matches the timing of earliest post-collisional granitic magmatism in the foreland at c. 630 Ma (Hartmann et al., 2002; Lara et al., 2017; Oyhantçabal et al., 2009), suggesting that these leucocratic veins may simply be minor dykes associated with early post-collisional melting in the foreland. Unfortunately, the poor outcrop situation and degree of deformation makes it difficult to accurately ascertain this

relationship in the field. It is likely that the c. 630 Ma melting, and perhaps all magmatism of this age in the Nico Pérez Terrane, reflects the end of early orogenic loading of the foreland, as these ages coincide with the timing of exhumation and cooling of the hinterland determined by K–Ar (Oyhantçabal et al., 2009). In any case, based on the monazite U–Pb concordia and  $^{208}\text{Pb}/^{232}\text{Th}$  weighted mean ages from the melanocratic part of the same sample (UC40:  $572.1 \pm 5.2$  Ma;  $574.9 \pm 7.6$  Ma), and a similar sample from the Campanero Unit (UF36:  $582.7 \pm 5.7$  Ma;  $572.1 \pm 7.8$  Ma), we infer that the dominant, pervasive high-T metamorphic event (D2) observed in these rocks most likely occurred between c. 585 and 570 Ma. This is c. 65–80 Ma after the high-T metamorphic event during early crustal thickening recorded in the hinterland Cerro Olivo Complex.

Based on the garnet Lu–Hf age from sample UE14B ( $582 \pm 23$  Ma), metamorphism in the Zanja del Tigre Formation similarly occurred c.  $60 \pm 20$  Ma after early crustal thickening and high-T metamorphism in the hinterland. Although the age is imprecise, it overlaps within error with the metamorphic ages from the Campanero Unit, suggesting that metamorphism in the Campanero and metasedimentary cover units was likely coeval. The estimated P–T conditions from the Schist Belt (samples UE14B and UD17, respectively) show that metamorphism in the metasedimentary cover units of the foreland followed a prograde path along an apparent geothermal gradient of  $\sim 25^{\circ}\text{C/km}$ , reaching lower-amphibolite facies at  $\sim 6$ – $7$  kbar and  $\sim 550$ – $560^{\circ}\text{C}$  (D2; Figure 14a). This contrasts with the high-T conditions recorded in the Campanero Unit. Metamorphism in the foreland at c. 580–570 Ma is contemporaneous with much of the post-collisional magmatic rocks intruding the Nico Pérez Terrane and adjacent shear zones (Lara et al., 2017; Oyhantçabal et al., 2007, 2009, 2012; Rapalini et al., 2015), suggesting that metamorphism may have been driven by thermal input from voluminous magmatic intrusions. However, despite the high apparent thermal gradient recorded in the Campanero Unit, the thermal gradient recorded in the metasedimentary cover units indicates prograde Barrovian-type metamorphism that is more consistent with tectonic burial than with the elevated geothermal gradients associated with thermal metamorphism (Figure 14). Furthermore, pre- to syn-tectonic garnet and staurolite growth in the metapelites show that metamorphism was contemporaneous with deformation. Thus, we interpret this metamorphic event to confirm observations in the field that the Campanero Unit is thrust over the metasedimentary cover units of the foreland, with the Campanero Unit representing a deep, hotter part of the foreland basement exhumed and

thrust over the more external foreland between c. 585 and 570 Ma (Figure 15c).

This thrusting event, from c. 585 Ma, is coeval with sinistral reactivation of major dextral orogen-parallel shear zones in the region. Sinistral deformation is recorded along the Sierra Ballena Shear Zone at  $586 \pm 2$  Ma (Oyhantçabal et al., 2009) and along the Sarandí del Yí Shear Zone at c. 595–585 (Oriolo et al., 2016; Oyhantçabal et al., 2009), which both show evidence of previous dextral movement from c. 630 Ma. However, based on the absence of clear asymmetric structures in many regions within the Sierra Ballena Shear Zone, and the presence of both sub-vertical and sub-horizontal stretching lineations, Oyhantçabal et al. (2009) described deformation in parts of the shear zone as predominantly pure-shear flattening within a sinistral transpressional system. Similar observations have been made in the Sarandí del Yí Shear Zone (Oyhantçabal et al., 2001; Oyhantçabal et al., 2007). This suggests highly variable strain partitioning during the extensive lifetime of the orogenic foreland.

## 7.2 | Tectonic implications

Our data support previous studies showing that peak metamorphism and associated melting in the hinterland occurred at roughly the same time everywhere along the Dom Feliciano Belt—in the Porto Belo, Várzea do Capivarita and Cerro Olivo complexes (Chemale et al., 2012; Lenz et al., 2011; Martil, 2016; Oyhantçabal et al., 2009)—as well as in the Coastal Terrane of the Kaoko Belt (Franz et al., 1999; Goscombe et al., 2005; Konopásek et al., 2008; Kröner et al., 2004; Seth et al., 1998). We also report, for the first time, evidence of the c. 655 Ma magmatic activity associated with early crustal thickening and high-T metamorphism in the southern Dom Feliciano Belt, which has otherwise only been recorded in the Porto Belo Complex and the Coastal Terrane (Chemale et al., 2012; Kröner et al., 2004; Seth et al., 1998). This result implies a tectonic environment already capable of sustaining high temperatures at c. 655 Ma. Furthermore, near-simultaneous crustal thickening along the hinterland of the Dom Feliciano Belt at the start of orogenesis implies the presence of converging continental crust eastward of the entire length of the orogen at c. 660–650 Ma (De Toni, Bitencourt, Nardi, et al., 2020; Lenz et al., 2011; Martil, 2016; Oyhantçabal et al., 2009; Percival et al., 2022; and this work). Thus, as the rift–drift transition between the Congo and Kalahari cratons did not start until c. 650 Ma (Hoffman, 2021), both the Kalahari and Congo cratons were likely involved in early orogenesis. The data therefore support the

interpretation that early crustal thickening and dextral transpression in the Dom Feliciano Belt was driven by high-angle to oblique convergence of the Congo and Kalahari cratons with the South American cratonic bodies (Rio de la Plata Craton, Luis Alves Craton, and Nico Pérez Terrane) by at least c. 660–650 Ma (Figure 15a).

Our data show that there is no record of coeval c. 650 Ma metamorphism in the Schist Belt of the southern Dom Feliciano Belt foreland, such as is seen in the Brusque and Porongos complexes of the northern and central foreland (Battisti, 2022; Percival et al., 2022). Instead, peak metamorphic conditions recorded in the southern foreland were reached between c. 585 and 570 Ma, during the later transpressional phase of orogenesis that affected both sides of the orogenic system, as it is recorded in foreland domains of the Dom Feliciano, Kaoko, and Gariep belts (Frimmel, 2018; Goscombe et al., 2003; Gresse, 1994; Hueck et al., 2018). There are two possible explanations for this discrepancy. Firstly, the record of early crustal thickening in the southern foreland may have been obliterated during the c. 580–570 Ma transpressional event. The imbrication of the foreland basement and oblique thrusting over the more distal parts of the foreland, and the subsequent metamorphism of the pre-orogenic sedimentary cover, could have led to the complete overprint of any previous metamorphic fabrics. Secondly, the currently exposed parts of the foreland supracrustal rocks may have never contained an earlier metamorphic record to begin with, potentially due to the foreland failing to reach the conditions needed for the development of a strong metamorphic overprint during early crustal thickening and subsequent tectonic burial. However, considering that the garnet-bearing metamorphic assemblage in the schists closest to the Campanero Unit (sample UE14B) appears to be coeval with the S2 transposition foliation, the S1 foliation likely represents an earlier fabric and thus the former scenario is the most likely. Although with no geochronological constraints for this earlier event, the interpretation remains speculative.

The c. 580 Ma sinistral transpressive event represents a switch from earlier, predominantly dextral shearing across the major orogen-parallel shear zones in the southern Dom Feliciano Belt, marking a significant geodynamic change within the orogen (Oriolo et al., 2016; Oriolo et al., 2016). This switch was potentially driven by the northward convergence of the Kalahari Craton with the Congo Craton from c. 580 Ma (Frimmel & Frank, 1998; Oriolo et al., 2016; Oyhantçabal et al., 2011; Rapela et al., 2011). This interpretation is supported by Hoffman (2021), who suggests that the Kalahari Craton continued to drift away from the Congo Craton after the end of rifting at c. 650 Ma, resulting in the opening of the

Damara basins. Basin closure and inversion occurred during the Damaran orogeny from c. 580 Ma, which is linked with convergence between the Coastal Terrane and Congo Craton (Lehmann et al., 2016) (Figure 15b,c).

In contrast with the southern Dom Feliciano Belt, sinistral deformation is almost completely absent from the major shear zones of the northern Dom Feliciano Belt, and there is only minor reactivation along these shear zones after c. 580 Ma (Hueck et al., 2018; Percival et al., 2022). Instead, it appears that deformation in the northern extension of the system at c. 580 Ma was confined almost completely to the eastern half of the orogen (Figure 15c). This was expressed by the development of the Kaoko Belt, where earliest metamorphism (east of the Coastal Terrane hinterland) is constrained to c. 580 Ma, and the main transpressional phase of orogenesis lasted until c. 550 Ma (Goscombe et al., 2003, 2005; Seth et al., 1998; Ulrich et al., 2011). Furthermore, just like in the southern Dom Feliciano Belt, sinistral transpression dominated in the Kaoko Belt during this time (Goscombe et al., 2003, 2005; Konopásek et al., 2005).

Thus, the data presented in this study support the hypothesis proposed by Oyhantçabal et al. (2011), whereby the c. 580 Ma sinistral transpressional reactivation of previous dextral shear structures in the Dom Feliciano Belt, as well as transpressional deformation in the Kaoko and Gariep belts, was driven by the oblique convergence of the Kalahari Craton (relative to the South American cratonic blocks). Deformation during this event was expressed more strongly in the southern and central Dom Feliciano Belt than in the north.

## 8 | CONCLUSIONS

- The foreland and hinterland domains of the southern Dom Feliciano Belt in Uruguay both show a dominating high-T deformation fabric (S1), with a generally E–W trending stretching lineation (L1) recorded in the basement complexes (Campanero Unit and Cerro Olivo Complex, respectively). S1 is overprinted by folds (F2) and an associated sub-vertical axial plane-parallel foliation (S2) containing a stretching lineation (L2) which are all oriented parallel to major N–S- to NE–SW-trending shear zones. The foreland basement differs slightly, showing also a sub-vertical E–W trending foliation (S3).
- Granulite facies rocks from the Cerro Olivo Complex (hinterland) record apparent peak metamorphism at  $\sim 9.5$ – $11.5$  kbar and  $\sim 760$ – $780^\circ\text{C}$ , and subsequent near-isothermal decompression down to  $\sim 5.5$ – $7.0$  kbar and  $\sim 770$ – $790^\circ\text{C}$ . A garnet Lu–Hf age of  $654 \pm 23$  Ma reflects the average age of garnet growth across these

two metamorphic stages, whereas a  $638.5 \pm 2.2$  Ma age records the timing of decompression-related, high-T metamorphism.


- A deformed porphyritic granite from the Cerro Olivo Complex records zircon U–Pb LA-ICP-MS and SIMS ages of  $656 \pm 4$  and  $654 \pm 3$  Ma, respectively, which reflects the igneous protolith age. The rock represents the first evidence of early orogenic magmatic activity in the Dom Feliciano Belt of Uruguay.
- Supracrustal rocks in the foreland Schist Belt record prograde metamorphism with a peak at 5.5–7.0 kbar and 550–575°C, and a garnet Lu–Hf age constrains this event to  $582 \pm 23$  Ma. Metamorphism in the Campanero Unit gneisses (foreland basement) reached peak conditions of 4–9 kbar and 670–770°C and is constrained by monazite U–Pb ages of  $582.7 \pm 5.7$  and  $572.1 \pm 5.2$  Ma. Metamorphism in the foreland was coeval with sinistral transpression recorded along major shear zones in the belt.
- The P–T–t paths recorded in the hinterland and foreland indicate (1) early west-directed imbrication and thrusting of the hinterland at c. 655–640 Ma (D1) and (2) late imbrication and thrusting of the foreland basement over the more distal supracrustal foreland rocks during sinistral transpression at c. 585–570 Ma (D2), c. 55–85 Ma after the start of crustal thickening recorded in the hinterland.
- This two-stage tectonic evolution event was likely driven by the three-way convergence between the Congo, Kalahari, and South American cratons.

## ACKNOWLEDGEMENTS

This work represents part of a PhD project which received financial support from the Norwegian Agency for International Cooperation and Quality Enhancement in Higher Education (Diku) and the Coordination for the Improvement of Higher Education Personnel (CAPES) (project no. UTF-2018-10004). J. Konopásek appreciates support from the Czech Science Foundation (project no. 18-24281S). Thanks to D. Sala and M. Koziarska for their help with isotopic analytical work, and R. Škoda and R. Čopjaková for assistance with microprobe analyses. We thank Martin Whitehouse and Heejin Jeon for their support while using the NordSIMS ion probe in Stockholm. The NordSIMS facility operated as a joint Nordic infrastructure, supported until 2014 by the research councils of Denmark, Norway, and Sweden (Swedish Research Council grant 2014-06375), and the Academy of Finland, and as Swedish national infrastructure (Swedish Research Council grant 2017-00671) since 2015, with additional support from the Swedish Museum of Natural History and the University of Iceland. This is NordSIMS publication #733.



## ORCID

Jack James Percival  <https://orcid.org/0000-0002-6542-7908>

Jiří Konopásek  <https://orcid.org/0000-0001-5625-3996>

Jiří Sláma  <https://orcid.org/0000-0002-1386-4196>

Robert Anczkiewicz  <https://orcid.org/0000-0001-6541-5192>

## REFERENCES

- Anczkiewicz, R., Chakraborty, S., Dasgupta, S., Mukhopadhyay, D., & Koltonik, K. (2014). Timing, duration and inversion of prograde Barrovian metamorphism constrained by high resolution Lu–Hf garnet dating: A case study from the Sikkim Himalaya, NE India. *Earth and Planetary Science Letters*, 407, 70–81. <https://doi.org/10.1016/j.epsl.2014.09.035>
- Anczkiewicz, R., Platt, J. P., Thirlwall, M. F., & Wakabayashi, J. (2004). Franciscan subduction off to a slow start: Evidence from high-precision Lu–Hf garnet ages on high grade-blocks. *Earth and Planetary Science Letters*, 225(1), 147–161. <https://doi.org/10.1016/j.epsl.2004.06.003>
- Anczkiewicz, R., & Thirlwall, M. F. (2003). Improving precision of Sm–Nd garnet dating by H<sub>2</sub>SO<sub>4</sub> leaching: A simple solution to the phosphate inclusion problem. *Geological Society, London, Special Publications*, 220(1), 83–91. <https://doi.org/10.1144/GSL.SP.2003.220.01.05>
- Anczkiewicz, R., Thirlwall, M., Alard, O., Rogers, N. W., & Clark, C. (2012). Diffusional homogenization of light REE in garnet from the day Nui con Voi massif in N-Vietnam: Implications for Sm–Nd geochronology and timing of metamorphism in the Red River shear zone. *Chemical Geology*, 318–319, 16–30. <https://doi.org/10.1016/j.chemgeo.2012.04.024>
- Bartoli, O. (2017). Phase equilibria modelling of residual migmatites and granulites: An evaluation of the melt-reintegration approach. *Journal of Metamorphic Geology*, 35(8), 919–942. <https://doi.org/10.1111/jmg.12261>
- Basei, M. A. S., Siga, O. Jr., Masquelin, H., Harara, O. M., Reis Neto, J. M., & Preciozzi, F. (2000). The Dom Feliciano Belt of Brazil and Uruguay and its Foreland Domain, the Rio de la Plata Craton: framework, tectonic evolution and correlation with similar provinces of Southwestern Africa. In U. G. Cordani, et al. (Eds.), *Tectonic evolution of South America* (pp. 311–334). Geological Society. <https://doi.org/10.13140/RG.2.1.5109.4567>
- Battisti, M. A. (2022). *Evolução geológica (800–560 Ma) do setor central do Cinturão Dom Feliciano com base no estudo petrológico, geocronológico e de proveniência dos complexos Porongos, Várzea do Capivara e Passo Feio, RS*. Universidade Federal do Rio Grande do Sul. Doctoral thesis, available at: <https://www.lume.ufrgs.br/handle/10183/239719>
- Battisti, M. A., Bitencourt, M. F., De Toni, G. B., Nardi, L. V. S., & Konopásek, J. (2018). Metavolcanic rocks and orthogneisses from Porongos and Várzea do Capivara complexes: A case for identification of tectonic interleaving at different crustal levels from structural and geochemical data in southernmost Brazil. *Journal of South American Earth Sciences*, 88, 253–274. <https://doi.org/10.1016/j.jsames.2018.08.009>
- Battisti, M. A., Bitencourt, M. F., Florisbal, L. M., Nardi, L. V. S., Ackerman, L., Sláma, J., & Padilha, D. F. (2023). Unravelling major magmatic episodes from metamorphic sequences of the Dom Feliciano Belt central sector, southernmost Brazil – A comparative study of geochronology, elemental geochemistry, and Sr–Nd data. *Precambrian Research*, 385, 106951. <https://doi.org/10.1016/j.precamres.2022.106951>
- Bitencourt, M. F., & Nardi, L. V. S. (2000). Tectonic setting and sources of magmatism related to the southern Brazilian shear belt. *Revista Brasileira de Geociências*, 30(1), 186–189. <https://doi.org/10.25249/0375-7536.2000301186189>
- Caddick, M., Konopásek, J., & Thompson, A. (2010). Preservation of garnet growth zoning and the duration of prograde metamorphism. *Journal of Petrology*, 51, 2327–2347. <https://doi.org/10.1093/petrology/egq059>
- Chemale, F. Jr., Mallmann, G., Bitencourt, M. F., & Kawashita, K. (2012). Time constraints on magmatism along the Major Gercino shear zone, southern Brazil: Implications for West Gondwana reconstruction. *Gondwana Research*, 22(1), 184–199. <https://doi.org/10.1016/j.gr.2011.08.018>
- Cheng, H. (2019). Garnet Lu–Hf and Sm–Nd geochronology: A time capsule of the metamorphic evolution of orogenic belts. *Geological Society, London, Special Publications*, 474(1), 47–67. <https://doi.org/10.1144/sp474.7>
- Chigliano, L., Gaucher, C., Sial, A. N., Bossi, J., Ferreira, V. P., & Pimentel, M. M. (2010). Chemostratigraphy of Mesoproterozoic and Neoproterozoic carbonates of the Nico Pérez terrane, Río de la Plata craton, Uruguay. *Precambrian Research*, 182(4), 313–336. <https://doi.org/10.1016/j.precamres.2010.06.002>
- Coelho, M. B., Trouw, R. A. J., Ganade, C. E., Vinagre, R., Mendes, J. C., & Sato, K. (2017). Constraining timing and P–T conditions of continental collision and late overprinting in the southern Brasília Orogen (SE-Brazil): U–Pb zircon ages and geothermobarometry of the Andreândia nappe system. *Precambrian Research*, 292(Supplement C), 194–215. <https://doi.org/10.1016/j.precamres.2017.02.001>
- Connolly, J. A. D. (2005). Computation of phase equilibria by linear programming: A tool for geodynamic modeling and its application to subduction zone decarbonation. *Earth and Planetary Science Letters*, 236(1–2), 524–541. <https://doi.org/10.1016/j.epsl.2005.04.033>
- De Toni, G. B., Bitencourt, M. F., Konopásek, J., Battisti, M. A., Oliveira da Costa, E., & Savian, J. F. (2021). Autochthonous origin of the Encruzilhada block, Dom Feliciano Belt, southern Brazil, based on aerogeophysics, image analysis and PT-paths. *JGeo*, 144, 101825. <https://doi.org/10.1016/j.jog.2021.101825>
- De Toni, G. B., Bitencourt, M. F., Konopásek, J., Martini, A., Andrade, P. H. S., Florisbal, L. M., & Campos, R. S. (2020). Transpressive strain partitioning between the Major Gercino shear zone and the Tijucas Fold Belt, Dom Feliciano Belt, Santa Catarina, southern Brazil. *Journal of Structural Geology*, 136, 104058. <https://doi.org/10.1016/j.jsg.2020.104058>
- De Toni, G. B., Bitencourt, M. F., Nardi, L. V. S., Florisbal, L. M., Almeida, B. S., & Geraldies, M. (2020). Dom Feliciano Belt orogenic cycle tracked by its pre-collisional magmatism: The Tonian (ca. 800 ma) Porto Belo complex and its correlations in southern Brazil and Uruguay. *Precambrian Research*, 342, 105702. <https://doi.org/10.1016/j.precamres.2020.105702>

- Dodson, M. H. (1973). Closure temperature in cooling geochronological and petrological systems. *Contributions to Mineralogy and Petrology*, 40(3), 259–274. <https://doi.org/10.1007/BF00373790>
- Franz, L., Romer, R. L., & Dingeldey, D. P. (1999). Diachronous pan-African granulite-facies metamorphism (650 ma and 550 ma) in the Kaoko Belt, NW Namibia. *European Journal of Mineralogy*, 11(1), 167–180. <https://doi.org/10.1127/ejm/11/1/0167>
- Frimmel, H. E. (2018). The Gariep Belt. In S. Siegesmund, et al. (Eds.), *Geology of Southwest Gondwana* (1st ed., pp. 353–386). Springer International Publishing. [https://doi.org/10.1007/978-3-319-68920-3\\_13](https://doi.org/10.1007/978-3-319-68920-3_13)
- Frimmel, H. E., & Frank, W. (1998). Neoproterozoic tectonothermal evolution of the Gariep Belt and its basement, Namibia and South Africa. *Precambrian Research*, 90(1), 1–28. [https://doi.org/10.1016/S0301-9268\(98\)00029-1](https://doi.org/10.1016/S0301-9268(98)00029-1)
- Fuhrman, M. L., & Lindsley, D. H. (1988). Ternary-feldspar modeling and thermometry. *American Mineralogist*, 73(3–4), 201–215.
- Ganguly, J., & Tirone, M. (1999). Diffusion closure temperature and age of a mineral with arbitrary extent of diffusion: Theoretical formulation and applications. *Earth and Planetary Science Letters*, 170(1), 131–140. [https://doi.org/10.1016/S0012-821X\(99\)00089-8](https://doi.org/10.1016/S0012-821X(99)00089-8)
- Gaucher, C., Frei, R., Chemale, F. Jr., Frei, D., Bossi, J., Martínez, G., Chigilino, L., & Cernuschi, F. (2011). Mesoproterozoic evolution of the Río de la Plata craton in Uruguay: At the heart of Rodinia? *International Journal of Earth Sciences*, 100(2), 273–288. <https://doi.org/10.1007/s00531-010-0562-x>
- Goscombe, B., Foster, D. A., Gray, D., & Wade, B. (2017). Metamorphic response and crustal architecture in a classic collisional orogen: The Damara Belt, Namibia. *Gondwana Research*, 50, 80–124. <https://doi.org/10.1016/j.gr.2017.07.006>
- Goscombe, B., Foster, D. A., Gray, D., & Wade, B. (2018). *The evolution of the Damara orogenic system: A record of West Gondwana assembly and crustal response*. In S. Siegesmund, M. A. S. Basei, P. Oyhantçabal & S. Oriolo (Eds.), *Geology of Southwest Gondwana* (pp. 303–352). Springer International Publishing. [https://doi.org/10.1007/978-3-319-68920-3\\_12](https://doi.org/10.1007/978-3-319-68920-3_12)
- Goscombe, B., Gray, D., Armstrong, R., Foster, D. A., & Vogl, J. (2005). Event geochronology of the pan-African Kaoko Belt, Namibia. *Precambrian Research*, 140(3–4), 103.e1–103.e41. <https://doi.org/10.1016/j.precamres.2005.07.003>
- Goscombe, B., Gray, D., & Hand, M. (2005). Extrusional tectonics in the Core of a Transpressional Orogen; the Kaoko Belt, Namibia. *Journal of Petrology*, 46(6), 1203–1241. <https://doi.org/10.1093/petrology/egi014>
- Goscombe, B., Hand, M., & Gray, D. (2003). Structure of the Kaoko Belt, Namibia: Progressive evolution of a classic transpressional orogen. *Journal of Structural Geology*, 25(7), 1049–1081. [https://doi.org/10.1016/S0191-8141\(02\)00150-5](https://doi.org/10.1016/S0191-8141(02)00150-5)
- Goscombe, B., Hand, M., Gray, D., & Mawby, J. O. (2003). The metamorphic architecture of a Transpressional Orogen: The Kaoko Belt, Namibia. *Journal of Petrology*, 44(4), 679–711. <https://doi.org/10.1093/petrology/44.4.679>
- Gresse, P. G. (1994). Strain partitioning in the southern Gariep arc as reflected by sheath folds and stretching directions. *South African Journal of Geology*, 97(1), 52–61.
- Gross, A. O. M. S., Droop, G. T. R., Porcher, C. C., & Fernandes, L. A. D. (2009). Petrology and thermobarometry of mafic granulites and migmatites from the Chafalote metamorphic suite: New insights into the Neoproterozoic P–T evolution of the Uruguayan–Sul-Rio-Grandense shield. *Precambrian Research*, 170(3–4), 157–174. <https://doi.org/10.1016/j.precamres.2009.01.011>
- Gross, A. O. M. S., Porcher, C. C., Fernandes, L. A. D., & Koester, E. (2006). Neoproterozoic low-pressure/high-temperature collisional metamorphic evolution in the Varzea do Capivarita metamorphic suite, SE Brazil: Thermobarometric and Sm/Nd evidence. *Precambrian Research*, 147(1), 41–64. <https://doi.org/10.1016/j.precamres.2006.02.001>
- Harrison, T. M., Célérier, J., Aikman, A. B., Hermann, J., & Heizler, M. T. (2009). Diffusion of <sup>40</sup>Ar in muscovite. *Geochimica et Cosmochimica Acta*, 73(4), 1039–1051. <https://doi.org/10.1016/j.gca.2008.09.038>
- Hartmann, L. A., Campal, N., Santos, J. O. S., McNaughton, N. J., Bossi, J., Schipilov, A., & Lafon, J.-M. (2001). Archean crust in the Río de la Plata craton, Uruguay — SHRIMP U–Pb zircon reconnaissance geochronology. *Journal of South American Earth Sciences*, 14(6), 557–570. [https://doi.org/10.1016/S0895-9811\(01\)00055-4](https://doi.org/10.1016/S0895-9811(01)00055-4)
- Hartmann, L. A., Santos, J. O. S., Bossi, J., Campal, N., Schipilov, A., & McNaughton, N. J. (2002). Zircon and titanite U–Pb SHRIMP geochronology of Neoproterozoic felsic magmatism on the eastern border of the Río de la Plata craton, Uruguay. *Journal of South American Earth Sciences*, 15(2), 229–236. [https://doi.org/10.1016/S0895-9811\(02\)00030-5](https://doi.org/10.1016/S0895-9811(02)00030-5)
- Heine, C., Zoethout, J., & Müller, R. D. (2013). Kinematics of the South Atlantic rift. *Solid Earth*, 4(2), 215–253. <https://doi.org/10.5194/se-4-215-2013>
- Hoffman, P. F. (2021). On the kinematics and timing of Rodinia breakup: A possible rift–transform junction of Cryogenian age at the southwest cape of Congo craton (Northwest Namibia). *South African Journal of Geology*, 124(2), 401–420. <https://doi.org/10.25131/sajg.124.0038>
- Holland, T. J. B., & Powell, R. (2011). An improved and extended internally consistent thermodynamic dataset for phases of petrological interest, involving a new equation of state for solids. *Journal of Metamorphic Geology*, 29(3), 333–383. <https://doi.org/10.1111/j.1525-1314.2010.00923.x>
- Hollister, L. S. (1966). Garnet zoning: An interpretation based on the Rayleigh fractionation model. *Science*, 154(3757), 1647–1651. <https://doi.org/10.1126/science.154.3757.1647>
- Holness, M., Cesare, B., & Sawyer, E. (2011). Melted rocks under the microscope: Microstructures and their interpretation. *Elements*, 11, 7–247. <https://doi.org/10.2113/gselements.7.4.247>
- Hueck, M., Basei, M. A. S., Wemmer, K., Oriolo, S., Heidelberg, F., & Siegesmund, S. (2018). Evolution of the Major Gercino shear zone in the Dom Feliciano Belt, South Brazil, and implications for the assembly of southwestern Gondwana. *International Journal of Earth Sciences*, 108(2), 403–425. <https://doi.org/10.1007/s00531-018-1660-4>
- Hueck, M., Oriolo, S., Basei, M. A. S., Oyhantçabal, P., Heller, B. M., Wemmer, K., & Siegesmund, S. (2022). Archean to early Neoproterozoic crustal growth of the southern south American platform and its wide-reaching “African” origins.

- Precambrian Research*, 369, 106532. <https://doi.org/10.1016/j.precamres.2021.106532>
- Hueck, M., Oyhantçabal, P., Basei, M., & Siegesmund, S. (2018). The Dom Feliciano Belt in Southern Brazil and Uruguay. In S. Siegesmund, et al. (Eds.), *Geology of Southwest Gondwana* (1st ed., pp. 267–302). Springer International Publishing. [https://doi.org/10.1007/978-3-319-68920-3\\_11](https://doi.org/10.1007/978-3-319-68920-3_11)
- Indares, A., White, R. W., & Powell, R. (2008). Phase equilibria modelling of kyanite-bearing anatectic paragneisses from the Central Grenville Province. *Journal of Metamorphic Geology*, 26(8), 815–836. <https://doi.org/10.1111/j.1525-1314.2008.00788.x>
- Kelly, E. D., Carlson, W. D., & Connelly, J. N. (2011). Implications of garnet resorption for the Lu–Hf garnet geochronometer: An example from the contact aureole of the Makhavinekh Lake pluton, Labrador. *Journal of Metamorphic Geology*, 29(8), 901–916. <https://doi.org/10.1111/j.1525-1314.2011.00946.x>
- Konopásek, J., Cavalcante, C., Fossen, H., & Janoušek, V. (2020). Adamastor – An ocean that never existed? *Earth Science Reviews*, 205, 103201. <https://doi.org/10.1016/j.earscirev.2020.103201>
- Konopásek, J., Hoffmann, K.-H., Sláma, J., & Košler, J. (2017). The onset of flysch sedimentation in the Kaoko Belt (NW Namibia) – Implications for the pre-collisional evolution of the Kaoko–Dom Feliciano–Gariiep orogen. *Precambrian Research*, 298, 220–234. <https://doi.org/10.1016/j.precamres.2017.06.017>
- Konopásek, J., Janoušek, V., Oyhantçabal, P., Sláma, J., & Ulrich, S. (2018). Did the circum-Rodinia subduction trigger the Neoproterozoic rifting along the Congo–Kalahari craton margin? *International Journal of Earth Sciences*, 107(5), 1859–1894. <https://doi.org/10.1007/s00531-017-1576-4>
- Konopásek, J., Košler, J., Tajčmanová, L., Ulrich, S., & Kitt, S. (2008). Neoproterozoic igneous complex emplaced along major tectonic boundary in the Kaoko Belt (NW Namibia): Ion probe and LA-ICP-MS dating of magmatic and metamorphic zircons. *Journal of the Geological Society of London*, 165(1), 153–165. <https://doi.org/10.1144/0016-76492006-192>
- Konopásek, J., Kröner, S., Kitt, S. L., Passchier, C. W., & Kröner, A. (2005). Oblique collision and evolution of large-scale transcurrent shear zones in the Kaoko belt, NW Namibia. *Precambrian Research*, 136(2), 139–157. <https://doi.org/10.1016/j.precamres.2004.10.005>
- Kröner, S., Konopásek, J., Kröner, A., Passchier, C. W., Poller, U., Wingate, M. T. D., & Hofmann, K. H. (2004). U–Pb and Pb–Pb zircon ages for metamorphic rocks in the Kaoko Belt of north-western Namibia: A Palaeo- to Mesoproterozoic basement reworked during the pan-African orogeny. *South African Journal of Geology*, 107(3), 455–476. <https://doi.org/10.2113/107.3.455>
- Lanari, P., & Engi, M. (2017). Local bulk composition effects on metamorphic mineral assemblages. *Reviews in Mineralogy and Geochemistry*, 83, 55–102. <https://doi.org/10.2138/rmg.2017.83.3>
- Lara, P., Oyhantçabal, P., & Dadd, K. (2017). Post-collisional, late Neoproterozoic, high-Ba–Sr granitic magmatism from the Dom Feliciano Belt and its cratonic foreland, Uruguay: Petrography, geochemistry, geochronology, and tectonic implications. *Lithos*, 277, 178–198. <https://doi.org/10.1016/j.lithos.2016.11.026>
- Larson, K. P., Shrestha, S., Soret, M., & Smit, M. (2020). The P–T–D evolution of the Mahabharat, east-Central Nepal: The out-of-sequence development of the Himalaya. *Geoscience Frontiers*, 13, 101057. <https://doi.org/10.1016/j.gsf.2020.08.001>
- Lehmann, J., Saalman, K., Naydenov, K. V., Milani, L., Belyanin, G. A., Zwingmann, H., Charlesworth, G., & Kinnaird, J. A. (2016). Structural and geochronological constraints on the pan-African tectonic evolution of the northern Damara Belt, Namibia. *Tectonics*, 35, 103–135. <https://doi.org/10.1002/2015TC003899>
- Lenz, C., Fernandes, L. A. D., McNaughton, N. J., Porcher, C. C., & Masquelin, H. (2011). U–Pb SHRIMP ages for the Cerro Bori Orthogneisses, Dom Feliciano Belt in Uruguay: Evidences of a ~800Ma magmatic and ~650Ma metamorphic event. *Precambrian Research*, 185(3), 149–163. <https://doi.org/10.1016/j.precamres.2011.01.007>
- Lenz, C., Porcher, C., Fernandes, L., Masquelin, H., Koester, E., & Conceição, R. (2013). Geochemistry of the Neoproterozoic (800–767 ma) Cerro Bori orthogneisses, Dom Feliciano Belt in Uruguay: Tectonic evolution of an ancient continental arc. *Mineralogy and Petrology*, 107, 785–806. <https://doi.org/10.1007/s00710-012-0244-4>
- Mallmann, G., Chemale, F. Jr., Ávila, J. N., Kawashita, K., & Armstrong, R. A. (2007). Isotope geochemistry and geochronology of the Nico Pérez terrane, Rio de la Plata craton, Uruguay. *Gondwana Research*, 12(4), 489–508. <https://doi.org/10.1016/j.gr.2007.01.002>
- Marmo, B. A., Clarke, G. L., & Powell, R. (2002). Fractionation of bulk rock composition due to porphyroblast growth: Effects on eclogite facies mineral equilibria, Pam Peninsula, New Caledonia. *Journal of Metamorphic Geology*, 20(1), 151–165. <https://doi.org/10.1046/j.0263-4929.2001.00346.x>
- Martil, M. M. D. (2016). *O Magmatismo De Arco Continental Pré-collisional (790 Ma) E a Reconstituição Espaço-temporal Do Regime Transpressivo (650 Ma) No Complexo Várzea Do Capivarita, Sul Da Província Mantiqueira*. Universidade Federal do Rio Grande do Sul. Doctoral thesis, available at: <https://www.lume.ufrgs.br/handle/10183/149194>
- Martil, M. M. D., Bitencourt, M. F., Nardi, L. V. S., Koester, E., & Pimentel, M. M. (2017). Pre-collisional, Tonian (ca. 790 ma) continental arc magmatism in southern Mantiqueira Province, Brazil: Geochemical and isotopic constraints from the Várzea do Capivarita complex. *Lithos*, 274–275, 39–52. <https://doi.org/10.1016/j.lithos.2016.11.011>
- Masquelin, H., Aífa, T., Scaglia, F., & Basei, M. A. S. (2021). The Archean Pavas block in Uruguay: Extension and tectonic evolution based on LA-ICP-MS U–Pb ages and airborne geophysics. *Journal of South American Earth Sciences*, 110, 103364. <https://doi.org/10.1016/j.jsames.2021.103364>
- Masquelin, H., Fernandes, L., Lenz, C., Porcher, C. C., & McNaughton, N. J. (2011). The Cerro Olivo complex: A pre-collisional Neoproterozoic magmatic arc in eastern Uruguay. *International Geology Review*, 54, 1161–1183. <https://doi.org/10.1080/00206814.2011.626597>
- McCourt, S., Armstrong, R., Jelsma, H., & Mapeo, R. (2013). New U–Pb SHRIMP ages from the Lubango region, SW Angola: Insights into the Palaeoproterozoic evolution of the Angolan shield, southern Congo craton, Africa. *Geological Society*



- Special Publication, 170(2), 353–363. <https://doi.org/10.1144/jgs2012-059>
- McDougall, I., & Harrison, T. M. (1999). *Geochronology and thermochronology by the  $^{40}\text{Ar}/^{39}\text{Ar}$  method*. Oxford University Press.
- Meira, V. T., Garcia-Casco, A., Hyppolito, T., Juliani, C., & Schorscher, J. H. D. (2019). Tectono-metamorphic evolution of the Central Ribeira Belt, Brazil: A case of late Neoproterozoic intracontinental orogeny and flow of partially molten deep crust during the assembly of West Gondwana. *Tectonics*, 38(8), 3182–3209. <https://doi.org/10.1029/2018tc004959>
- Oriolo, S., Oyhantçabal, P., Basei, M. A. S., Wemmer, K., & Siegesmund, S. (2016). The Nico Pérez terrane (Uruguay): From Archean crustal growth and connections with the Congo craton to late Neoproterozoic accretion to the Río de la Plata craton. *Precambrian Research*, 280, 147–160. <https://doi.org/10.1016/j.precamres.2016.04.014>
- Oriolo, S., Oyhantçabal, P., Heidelbach, F., Wemmer, K., & Siegesmund, S. (2015). Structural evolution of the Sarandí del Yí shear zone, Uruguay: Kinematics, deformation conditions and tectonic significance. *GR Geologische Rundschau*, 104(7), 1759–1777. <https://doi.org/10.1007/s00531-015-1166-2>
- Oriolo, S., Oyhantçabal, P., Konopásek, J., Basei, M. A. S., Frei, R., Sláma, J., Wemmer, K., & Siegesmund, S. (2019). Late Paleoproterozoic and Mesoproterozoic magmatism of the Nico Pérez terrane (Uruguay): Tightening up correlations in southwestern Gondwana. *Precambrian Research*, 327, 296–313. <https://doi.org/10.1016/j.precamres.2019.04.012>
- Oriolo, S., Oyhantçabal, P., Wemmer, K., Basei, M. A. S., Benowitz, J., Pfänder, J., Hannich, F., & Siegesmund, S. (2016). Timing of deformation in the Sarandí del Yí shear zone, Uruguay: Implications for the amalgamation of western Gondwana during the Neoproterozoic Brasiliano-pan-African orogeny. *Tectonics*, 35(3), 754–771. <https://doi.org/10.1002/2015tc004052>
- Oriolo, S., Oyhantçabal, P., Wemmer, K., Heidelbach, F., Pfänder, J., Basei, M. A. S., Hueck, M., Hannich, F., Sperner, B., & Siegesmund, S. (2016). Shear zone evolution and timing of deformation in the Neoproterozoic transpressional Dom Feliciano Belt, Uruguay. *Journal of Structural Geology*, 92, 59–78. <https://doi.org/10.1016/j.jsg.2016.09.010>
- Oyhantçabal, P., Heimann, A., & Miranda, S. (2001). Measurement and interpretation of strain in the syntectonic Solís de Mataojo granitic complex, Uruguay. *Journal of Structural Geology*, 23(5), 807–817. [https://doi.org/10.1016/S0191-8141\(00\)00152-8](https://doi.org/10.1016/S0191-8141(00)00152-8)
- Oyhantçabal, P., Oriolo, S., Philipp, R. P., Wemmer, K., & Siegesmund, S. (2018). The Nico Pérez Terrane of Uruguay and Southeastern Brazil. In S. Siegesmund, et al. (Eds.), *Geology of Southwest Gondwana* (pp. 161–188). Springer International Publishing. [https://doi.org/10.1007/978-3-319-68920-3\\_7](https://doi.org/10.1007/978-3-319-68920-3_7)
- Oyhantçabal, P., Oriolo, S., Wemmer, K., Basei, M. A. S., Frei, D., & Siegesmund, S. (2021). Provenance of metasedimentary rocks of the western Dom Feliciano Belt in Uruguay: Insights from U–Pb detrital zircon geochronology, Hf and Nd model ages, and geochemical data. *Journal of South American Earth Sciences*, 108, 103139. <https://doi.org/10.1016/j.jsames.2020.103139>
- Oyhantçabal, P., Siegesmund, S., & Wemmer, K. (2011). The Río de la Plata craton: A review of units, boundaries, ages and isotopic signature. *International Journal of Earth Sciences*, 100(2), 201–220. <https://doi.org/10.1007/s00531-010-0580-8>
- Oyhantçabal, P., Siegesmund, S., Wemmer, K., Frei, R., & Layer, P. (2007). Post-collisional transition from calc-alkaline to alkaline magmatism during transcurrent deformation in the southernmost Dom Feliciano Belt (Braziliano–pan-African, Uruguay). *Lithos*, 98(1–4), 141–159. <https://doi.org/10.1016/j.lithos.2007.03.001>
- Oyhantçabal, P., Siegesmund, S., Wemmer, K., & Layer, P. (2009). The sierra Ballena shear zone in the southernmost Dom Feliciano Belt (Uruguay): Evolution, kinematics, and deformation conditions. *International Journal of Earth Sciences*, 99(6), 1227–1246. <https://doi.org/10.1007/s00531-009-0453-1>
- Oyhantçabal, P., Siegesmund, S., Wemmer, K., & Passchier, C. W. (2011). The transpressional connection between Dom Feliciano and Kaoko belts at 580–550 ma. *International Journal of Earth Sciences*, 100, 379–390. <https://doi.org/10.1007/s00531-010-0577-3>
- Oyhantçabal, P., Siegesmund, S., Wemmer, K., Presnyakov, S., & Layer, P. (2009). Geochronological constraints on the evolution of the southern Dom Feliciano Belt (Uruguay). *Journal of the Geological Society*, 166(6), 1075–1084. <https://doi.org/10.1144/0016-76492008-122>
- Oyhantçabal, P., Wagner-Eimer, M., Wemmer, K., Schulz, B., Frei, R., & Siegesmund, S. (2012). Paleo- and Neoproterozoic magmatic and tectonometamorphic evolution of the Isla Cristalina de Rivera (Nico Pérez terrane, Uruguay). *International Journal of Earth Sciences*, 101(7), 1745–1762. <https://doi.org/10.1007/s00531-012-0757-4>
- Percival, J. J., Konopásek, J., Anczkiewicz, R., Ganerød, M., Sláma, J., Sacks de Campos, R., & Bitencourt, M. F. (2022). Tectono-metamorphic evolution of the northern Dom Feliciano Belt foreland, Santa Catarina, Brazil: Implications for models of subduction-driven orogenesis. *Tectonics*, 41, e2021TC007014. <https://doi.org/10.1029/2021TC007014>
- Percival, J. J., Konopásek, J., Eiesland, R., Sláma, J., de Campos, R. S., Battisti, M. A., & Bitencourt, M. d. F. (2021). Pre-orogenic connection of the foreland domains of the Kaoko–Dom Feliciano–Gariép orogenic system. *Precambrian Research*, 354, 106060. <https://doi.org/10.1016/j.precamres.2020.106060>
- Pertille, J., Hartmann, L. A., Santos, J. O. S., McNaughton, N. J., & Armstrong, R. (2017). Reconstructing the Cryogenian–Ediacaran evolution of the Porongos fold and thrust belt, southern Brasiliano Orogen, based on zircon U–Pb–Hf–O isotopes. *International Geology Review*, 59(12), 1532–1560. <https://doi.org/10.1080/00206814.2017.1285257>
- Preciozzi, F., Masquelin, H., & Basei, M. (1999). *The Namaqua–Grenville terrane of eastern Uruguay*. In: *2nd south American symposium on isotope geology* (pp. 338–340). October 1999, Villa Carlos Paz, Cordoba, Argentina.
- Rapalini, A. E., Tohver, E., Bettucci, L. S., Lossada, A. C., Barcelona, H., & Pérez, C. (2015). The late Neoproterozoic sierra de las Ánimas magmatic complex and playa Hermosa formation, southern Uruguay, revisited: Paleogeographic implications of new paleomagnetic and precise geochronologic data. *Precambrian Research*, 259, 143–155. <https://doi.org/10.1016/j.precamres.2014.11.021>

- Rapela, C. W., Fanning, C. M., Casquet, C., Pankhurst, R. J., Spalletti, L., Poiré, D., & Baldo, E. G. (2011). The Rio de la Plata craton and the adjoining pan-African/brasiliano terranes: Their origins and incorporation into south-West Gondwana. *Gondwana Research*, 20(4), 673–690. <https://doi.org/10.1016/j.gr.2011.05.001>
- Rossini, C. A., & Legrand, J. M. (2003). Tecto-metamorphic events in the Carapé group: A model for its Neoproterozoic evolution. *Revista de la Sociedad Uruguaya de Geología*, 1, 49–67.
- Saalmann, K., Gerdes, A., Lahaye, Y., Hartmann, L., Remus, M., & Läufer, A. (2011). Multiple accretion at the eastern margin of the Rio de la Plata craton: The prolonged Brasiliano orogeny in southernmost Brazil. *International Journal of Earth Sciences*, 100, 355–378. <https://doi.org/10.1007/s00531-010-0564-8>
- Sánchez, B. L., Cosarinsky, M., & Ramos, V. A. (2001). Tectonic setting of the late Proterozoic Lavalleya group (Dom Feliciano Belt), Uruguay. *Gondwana Research*, 4(3), 395–407. [https://doi.org/10.1016/S1342-937X\(05\)70339-7](https://doi.org/10.1016/S1342-937X(05)70339-7)
- Sánchez-Bettucci, L., Oyhançabal, P., Loureiro, J., Ramos, V. A., Preciozzi, F., & Basei, M. A. S. (2004). Mineralizations of the Lavalleya group (Uruguay), a probable Neoproterozoic volcano-sedimentary sequence. *Gondwana Research*, 7(3), 745–751. [https://doi.org/10.1016/S1342-937X\(05\)71060-1](https://doi.org/10.1016/S1342-937X(05)71060-1)
- Scherer, E. E., Cameron, K. L., & Blichert-Toft, J. (2000). Lu–Hf garnet geochronology: Closure temperature relative to the Sm–Nd system and the effects of trace mineral inclusions. *Geochimica et Cosmochimica Acta*, 64(19), 3413–3432. [https://doi.org/10.1016/S0016-7037\(00\)00440-3](https://doi.org/10.1016/S0016-7037(00)00440-3)
- Scherer, E. E., Munker, C., & Mezger, K. (2001). Calibration of the lutetium–hafnium clock. *Science*, 293(5530), 683–687. <https://doi.org/10.1126/science.1061372>
- Schulmann, K., Konopásek, J., Janoušek, V., Lexa, O., Lardeaux, J.-M., Edel, J.-B., Štípská, P., & Ulrich, S. (2009). An Andean type Palaeozoic convergence in the bohemian massif. *Comptes Rendus Geoscience*, 341(2), 266–286. <https://doi.org/10.1016/j.crte.2008.12.006>
- Schulz, B. (2021). Monazite microstructures and their interpretation in Petrochronology. *Frontiers. Earth Science*, 9, 668566. <https://doi.org/10.3389/feart.2021.668566>
- Seth, B., Kröner, A., Mezger, K., Nemchin, A. A., Pidgeon, R. T., & Okrusch, M. (1998). Archaean to Neoproterozoic magmatic events in the Kaoko belt of NW Namibia and their geodynamic significance. *Precambrian Research*, 92(4), 341–363. [https://doi.org/10.1016/S0301-9268\(98\)00086-2](https://doi.org/10.1016/S0301-9268(98)00086-2)
- Spoturno, J. J., Loureiro, J., Oyhançabal, P., & Pascale, A. (2012). *Mapa geológico del Departamento de Maldonado escala 1: 100,000*. Facultad de Ciencias (UdelaR)-Dirección Nacional de Minería y Geología (MIEM).
- Spoturno, J. J., Oyhançabal, P., & Faraone, M. (2019). *Mapa geológico del Departamento de Lavalleya escala 1:100,000*. Facultad de Ciencias (UdelaR)-Ministerio de Industria, Energía Y Minería (MIEM).
- Štípská, P., Schulmann, K., & Kröner, A. (2004). Vertical extrusion and middle crustal spreading of omphacite granulite: A model of syn-convergent exhumation (bohemian massif, Czech Republic). *Journal of Metamorphic Geology*, 22, 179–198. <https://doi.org/10.1111/j.1525-1314.2004.00508.x>
- Stüwe, K., & Powell, R. (1995). PT paths from modal proportions: Application to the Koralm complex, eastern Alps. *Contributions to Mineralogy and Petrology*, 119(1), 83–93. <https://doi.org/10.1007/BF00310719>
- Tajčmanová, L., Konopásek, J., & Schulmann, K. (2006). Thermal evolution of the orogenic lower crust during exhumation within a thickened Moldanubian root of the Variscan belt of Central Europe. *Journal of Metamorphic Geology*, 24(2), 119–134. <https://doi.org/10.1111/j.1525-1314.2006.00629.x>
- Ulrich, S., Konopásek, J., Jeřábek, P., & Tajčmanová, L. (2011). Transposition of structures in the Neoproterozoic Kaoko Belt (NW Namibia) and their absolute timing. *International Journal of Earth Sciences*, 100(2), 415–429. <https://doi.org/10.1007/s00531-010-0573-7>
- White, R. W., Powell, R., & Clarke, G. L. (2002). The interpretation of reaction textures in Fe-rich metapelitic granulites of the Musgrave block, Central Australia: Constraints from mineral equilibria calculations in the system K<sub>2</sub>O–FeO–MgO–Al<sub>2</sub>O<sub>3</sub>–SiO<sub>2</sub>–H<sub>2</sub>O–TiO<sub>2</sub>–Fe<sub>2</sub>O<sub>3</sub>. *Journal of Metamorphic Geology*, 20(1), 41–55. <https://doi.org/10.1046/j.0263-4929.2001.00349.x>
- White, R. W., Powell, R., & Halpin, J. A. (2004). Spatially-focussed melt formation in aluminous metapelites from Broken Hill, Australia. *Journal of Metamorphic Geology*, 22(9), 825–845. <https://doi.org/10.1111/j.1525-1314.2004.00553.x>
- White, R. W., Powell, R., Holland, T. J. B., Johnson, T. E., & Green, E. C. R. (2014). New mineral activity–composition relations for thermodynamic calculations in metapelitic systems. *Journal of Metamorphic Geology*, 32(3), 261–286. <https://doi.org/10.1111/jmg.12071>
- White, R. W., Powell, R., Holland, T. J. B., & Worley, B. A. (2000). The effect of TiO<sub>2</sub> and Fe<sub>2</sub>O<sub>3</sub> on metapelitic assemblages at greenschist and amphibolite facies conditions: Mineral equilibria calculations in the system K<sub>2</sub>O–FeO–MgO–Al<sub>2</sub>O<sub>3</sub>–SiO<sub>2</sub>–H<sub>2</sub>O–TiO<sub>2</sub>–Fe<sub>2</sub>O<sub>3</sub>. *Journal of Metamorphic Geology*, 18(5), 497–511. <https://doi.org/10.1046/j.1525-1314.2000.00269.x>
- Whitney, D., & Evans, B. (2010). Abbreviations for names of rock-forming minerals. *American Mineralogist*, 95, 185–187. <https://doi.org/10.2138/am.2010.3371>
- Will, T. M., Gaucher, C., Ling, X. X., Li, X. H., Li, Q. L., & Frimmel, H. E. (2019). Neoproterozoic magmatic and metamorphic events in the Cuchilla Dionisio terrane, Uruguay, and possible correlations across the South Atlantic. *Precambrian Research*, 320, 303–322. <https://doi.org/10.1016/j.precamres.2018.11.004>
- Will, T. M., Höhn, S., Frimmel, H. E., Gaucher, C., le Roux, P. J., & Macey, P. H. (2020). Petrological, geochemical and isotopic data of Neoproterozoic rock units from Uruguay and South Africa: Correlation of basement terranes across the South Atlantic. *Gondwana Research*, 80, 12–32. <https://doi.org/10.1016/j.gr.2019.10.012>

## SUPPORTING INFORMATION

Additional supporting information can be found online in the Supporting Information section at the end of this article.

**Text S1.** Analytical Methods

**Table S1.** Representative mineral analyses and recalculated compositions (samples UE08, UC73 and UB02).

**Table S2.** Representative mineral analyses and recalculated compositions (samples UD17, UE14B and UC40).

**Table S3.** Representative mineral analyses and recalculated compositions (sample UB22).

**Table S4.** Summary of estimated PT conditions and comparison of observed vs. modelled mineral compositional parameters based on mean PT values (indication of the goodness of intersection of mineral isopleths)

**Table S5.** Zircon LA-ICP-MS U-(Th)-Pb analytical details (template according to Horstwood et al. 2016)

**Data S1.** Supporting Information

**Data S2.** Supporting Information

**Data S3.** Supporting Information

**Data S4.** Supporting Information

**Data S5.** Supporting Information

**How to cite this article:** Percival, J. J., Konopásek, J., Oyhantçabal, P., Sláma, J., & Anczkiewicz, R. (2023). Garnet growth and mineral geochronology constrains the diachronous Neoproterozoic convergent evolution of the southern Dom Feliciano Belt, Uruguay. *Journal of Metamorphic Geology*, 41(7), 997–1030. <https://doi.org/10.1111/jmg.12734>